Fall 12-20-2020

Modeling of Non-Newtonian Fluid Flow in a Porous Medium

Hamza Azzam
University of Maine, hamza.azzam@maine.edu

MODELING OF NON-NEWTONIAN FLUID FLOW IN A POROUS MEDIUM

By

Hamza Azzam

B.Sc. Cairo University, 2017

A THESIS

Submitted in Partial Fulfillment of the

Requirements for the Degree of

Master of Science

(in Mechanical Engineering)

The Graduate School

The University of Maine

December 2020

Advisory Committee:

Zhihe Jin, Professor of Mechanical Engineering, Advisor

Richard Kimball, Professor of Mechanical Engineering

Yingchao Yang, Assistant Professor of Mechanical Engineering

MODELING OF NON-NEWTONIAN FLUID FLOW IN A POROUS MEDIUM

By

Hamza Azzam

Thesis Advisor: Dr. Zhihe Jin

An Abstract of the Thesis Presented
in Partial Fulfillment of the Requirements for the
Degree of Master of Science
(in Mechanical Engineering)
December 2020

Flows of Newtonian and non-Newtonian fluids in porous media are of considerable interest in several diverse areas, including petroleum engineering, chemical engineering, and composite materials manufacturing.

In the first part of this thesis, one-dimensional linear and radial isothermal infiltration models for a non-Newtonian fluid flow in a porous solid preform are presented. The objective is to investigate the effects of the flow behavior index, preform porosity and the inlet boundary condition (which is either a known applied pressure or a fluid flux factor) on the infiltration front, pore pressure distribution, and fluid content variation. In the second part of the thesis, a one-dimensional linear non-isothermal infiltration model for a Newtonian fluid is presented. The goal is to investigate the effects of convection heat transfer and the applied boundary conditions, which are the applied pressure and the inlet temperature, on the infiltration front, pore pressure distribution, temperature variation, and fluid content variation.

For all types of infiltrations studied in this thesis, the governing equations for the three-dimensional (3D) infiltration are first presented. The 3D equations are then reduced to those for one-dimensional (1D) flow. After that, self-similarity solutions are derived for the various types

of 1D flows. Finally, numerical results are presented and discussed for a ceramic solid preform infiltrated by a melted polymer liquid. The theoretical models and numerical results show that

1. For 1-D linear isothermal infiltration of a non-Newtonian fluid, the dimensional infiltration front varies with time according to $t^{\frac{n}{n+1}}$, where n is the flow behavior index. The dimensionless infiltration front increases with an increase in the flow behavior index n, and decreases with an increase in the porosity of the porous solid. The pore pressure varies almost linearly from the inlet to the infiltration front. The fluid content variation becomes negative when the non-dimensional distance reaches about 55% of the infiltration front.
2. For 1-D radial isothermal infiltration of a non-Newtonian fluid, the dimensional infiltration front varies with time according to $t^{\frac{n}{n+1}}$. The dimensionless infiltration front increases with an increase in the flow behavior index n, and decreases with an increase in the porosity of the porous solid. The pore pressure varies non-linearly from the inlet and reaches zero at the infiltration front.
3. The fluid travels farther in the linear infiltration than in the radial infiltration.
4. For 1-D linear non-isothermal infiltration of a Newtonian fluid, the dimensional infiltration front varies with time according to $t^{\frac{1}{2}}$. It appears that the convection has a negligible effect on the infiltration front and the pore pressure distribution. The infiltration front increases with a decrease in the porosity of the porous solid. The pore pressure varies almost linearly from the inlet to the infiltration front, where it reaches zero. With an applied temperature drop at the inlet, the temperature variation increases with increasing distance from the inlet and reaches zero at a distance farther than the infiltration front, not at the infiltration front.

ACKNOWLEDGEMENTS

I would like to acknowledge my advisor, Prof. Zhihe Jin, for providing guidance, advising and feedback throughout this thesis. I would also like to thank Prof. Richard Kimball and Prof. Yingchao Yang for serving on my committee and for their comments.

I am, as always, extremely grateful to my parents, who supported me with love and encouragement throughout my entire life. Without them, I could never achieve any success in my life.

In addition, I would like to thank Maine Space Grant Consortium and the Department of Mechanical Engineering at the University of Maine for their financial support.

Finally, I would like to thank everyone who played a rule in this accomplishment.

TABLE OF CONTENTS

LIST OF TABLES

LIST OF FIGURES

LIST OF SYMBOLS

Symbol	Description
α	Biot–Willis coefficient
α_f	Volumetric thermal expansion coefficient of the fluid
α_s	Volumetric thermal expansion coefficient of the preform
A	Cross section area
B	Skempton's coefficient
c_p	Porous medium compressibility coefficient
c_f	Fluid compressibility coefficient
c	Specific heat
c_0	Total compressibility coefficient in the flow region
δ_{ij}	Kronecker delta
∇^2	Laplacian operator
ε	Strain
η	Dimensionless distance
η_f	Dimensionless infiltration front
η_w	Hole dimensionless distance
υ	Drained Poisson's ratio
f	Body force per unit volume of fluid
F	Body force per unit volume of the bulk material
G	Shear modulus of the drained elastic solid
g	Gravity component

H	Consistency index
h	Heat flux
h	Hole thickness
r_w	Hole radius
K	Drained Bulk modulus
κ	Permeability coefficient or mobility coefficient
k_α	Thermal conductivity of the fluid phase
k	Intrinsic permeability
λ	Thermal conductivity
Q_w	Inlet flow rate
M_α	Connectivity matrix of the fluid phase
M_β	Connectivity matrix of the solid phase
n	Flow behavior index
μ_{eff}	Effective viscosity of the fluid
σ	Stress
p_0	Applied inlet pressure
$\tilde{p}$	Dimensionless pore pressure
p	Pore pressure
ϕ_0	Porosity
q_{fs}	Convection induced heat transfer
q	Fluid flux

Q_0	Injection intensity
Q_o	Injection intensity
r_f	Infiltration front radius
θ	Temperature variation
$\tilde{\theta}$	Dimensionless temperature variation
θ_0	Inlet temperature
t	Time
u	Displacement
x_f	Infiltration front distance
ζ	Variation of fluid content

1 INTRODUCTION

Newtonian and non-Newtonian fluid flows through porous media are of considerable interest in several diverse areas; these areas include petroleum, chemical and environmental engineering, and composite materials manufacturing.

In petroleum engineering, the oil displacement efficiency is improved by using non-Newtonian displacing fluids [1,2]. Therefore, non-Newtonian fluids, such as shear-thinning polymer solutions [3,4,5], microemulsions, macroemulsions, and foam solutions [6], are injected into underground reservoir to improve the efficiency of oil displacement. Another example for applications in petroleum engineering is the production of heavy crude oils, where the rheological studies indicated that some of them are also non-Newtonian fluids of power law with yield stress [7,8,9].

For chemical, environmental, and biomedical engineering applications, non-Newtonian fluid flow in porous media is applied to the filtration of polymer solutions, soil remediation [10], food processing [11], and fermentation, through the removal of liquid pollutants. These fluids occur in many natural and synthetic forms and can be regarded as the rule not the exception [12]. Also, during water flooding operations, chemical additives, polymeric solutions, or foams are routinely added to the injected water for improving the overall sweeping efficiency and minimizing the instability effects. Surfactants are also added to the water phase to decrease the surface tension between the aqueous and oil phases [13]. Another application is the fluid flow in fixed and fluidised beds of particles, which is encountered in many chemical and processing applications [16]. In addition, the aqueous solutions of Separan AP-30, polymethylcellulose, and polyvinylpyrrolidone were found to exhibit non-Newtonian flow behavior in simple shear [15]. In environmental engineering, liquid pollutants and wastes may migrate in the subsurface and

penetrate underground reservoirs, leading to groundwater contamination; several of those, such as suspensions, solutions and emulsions of various substances, certain asphalts and bitumen, greases, sludges, and slurries, are distinctly non-Newtonian [13]. In Orthopaedic applications, Injectable bone cements (IBCs) are used in many applications, like poly methyl methacrylate (PMMA), where bone cements are used for anchoring total joint replacements (TJRs) [14].

In composite materials production, the infiltration process, which is the method of replacing a fluid (usually vacuum of gas) by another fluid within the pore space of a porous solid material [20], is being used to manufacture metal matrix composites (MMCs) [5,17], polymer matrix composites (PMCs) [18,19] and ceramic matrix composites (CMCs) [20,21]. In general, composites fabrication by infiltration method is one of the most cost-effective and efficient ways available for many reinforced composite (MMCs, PMCs, or CMCs) [20,22]. An example for the properties of the CMCs manufactured by infiltration was shown in [23], where SEM observations of the indentation induced cracks indicated that the polymer network causes much greater crack deflection than the dense ceramic material.

Flows of Newtonian and non-Newtonian fluids through porous media can be studied by analytical, numerical, and experimental methods. Many authors have carried out the analytical studies in flow applications.

In Petroleum Engineering related studies, Pascal [24,25] showed the basic equations describing the flow through a porous medium of non-Newtonian fluids with a power-law in the presence of a yield stress. Pascal, also, presented a theoretical analysis for evaluating the effects of non-Newtonian behavior of the displacing fluid on the interface stability in a radial displacement in a porous medium and presented some results that demonstrates the theoretical support for the finding of a strategy regarding the optimal selection of rheological parameters of the displacing

fluid. While in [26], Pascal developed approximate analytical solutions for the description of conditions required for the stability of non-Newtonian fluid interfaces in a porous medium. Pascal also studied the rheological effects of non-Newtonian fluids in a flow system of a two-phase flow zone, which are coupled to a single-phase flow zone by a moving fluid interface. The mentioned flow system is involved in a technique for oil displacement in a porous medium. In addition, Pascal showed the effects of non-Newtonian displacing fluids, of power law with yield stress, rheological on the dynamics of a moving interface, which occurs in separating oil from water. Several relevant conclusions, obtained there, illustrated the conditions in which the viscous fingering effect in oil displacement could be eliminated and a piston-like displacement may be possible [27,28]. In addition, Pascal analyzed the non-linear effects associated with unsteady flows through a porous medium of shear thinning fluids. He showed the existence of a moving pressure front from a self-similar solution governing the flow behavior. Pascal concluded that the pressure disturbances in a non-Newtonian fluid flowing through a porous medium propagate with a finite velocity. This relevant result is in contrast to the infinite velocity of disturbance propagation in a Newtonian fluid [29]. Finally, in another study, H. Pascal and F. Pascal [30] presented a study related to the solutions of the nonlinear equations of fluid flow in porous media. These solutions were obtained by means of a generalized Boltzmann transformation approach for several cases of practical interest in interpretation of well-flow tests of short duration. They also showed and discussed the limitations associated with the generalized Boltzmann transformation approach in solving the nonlinear equations of power law fluid flow in oil reservoirs taking into account the interpretation of the well-flow test analysis. A formulation of moving boundary problems occurring in the flow-test analysis of short duration enabled them to obtain the exact analytical solutions in certain cases of practical interest, like the case of a known constant inlet pressure. However, some limitations

associated with the generalized Boltzmann transformation approach arised when the boundary condition imposed (at the well) was expressed in terms of flow rate instead of a constant pressure. In that case, the solution in the closed form was obtained only for a certain profile of variable flow rate in the well.

Chen et al. [33] presented a class of self-similar solutions describing piston-like displacement of a slightly compressible non-Newtonian, power-law, dilatant fluid by another through a homogeneous, isotropic porous medium. Their solutions could be used to evaluate the validity and accuracy of approximate solutions that were existed.

Federico et al. [34] presented a simplified approach to the derivation of an effective permeability for flow of a purely viscous power–law fluid with flow behavior index n in a randomly heterogeneous porous domain subjected to a uniform pressure gradient. They concluded that in 1-D flow, the ratio between effective and mean permeability decreases with increasing heterogeneity, with a moderate impact of the flow behavior index value, while in 2-D and 3-D flows, the ratio between effective and mean permeability decreases with increasing log-permeability variance, except for very pseudoplastic fluids with a flow behavior index smaller than a limit value depending on flow dimensionality.

Federico and Ciriello [13] also analyzed the dynamics of the pressure variation generated by an instantaneous mass injection in the origin of a domain, initially saturated by a weakly compressible non-Newtonian fluid. Coupling the flow law, which is the modified Darcy's law, with the mass balance equation yielded the nonlinear partial differential equation governing the pressure field. After that, an analytical solution was derived as a function of a self-similar variable. Federico and Ciriello revealed in their analysis that the compressibility coefficient and flow behavior index are the most influential variables affecting the front position; when the excess

pressure is considered, compressibility and permeability coefficients contribute most to the total response variance. For both output variables the influence of the uncertainty in the porosity is decidedly lower. Federico and Ciriello analytically examined the dynamics of pressure diffusion in unsteady non-Newtonian flows, generated within the domain by an instantaneous mass injection in its origin, through porous media. They also introduced a self-similar variable and obtained a generalized closed-form solution in a dimensionless form, valid for plane, cylindrical, and semi-spherical geometry, and found that the variables of interest are functions of flow geometry, injected mass, fluid behavior index and dimensionless compressibility, and medium porosity. Federico and Ciriello confirmed the existence of a pressure front traveling with finite velocity for pseudoplastic fluids, and showed that the front advances farther in plane than in cylindrical or semi-spherical geometry; for a lower porosity, a larger flow behavior index, a lower compressibility, and a higher injected mass. A global sensitivity analysis (GSA) was conducted considering the fluid flow behavior index, and selected domain properties as independent random variables having uniform distributions. They stated that the compressibility coefficient is the most influential variable affecting the evolution of the front position with time, then the flow behavior index. The variation in space of the excess pressure at a given time is most affected by the permeability near the injection point, while the influence of the compressibility prevails closer to the front position.

In addition, Federico and Ciriello [38] performed an analytical analysis to interpret the key phenomena involved in non-Newtonian displacement in porous media, by considering the uncertainty associated with relevant problem parameters. The radial dynamics of a moving stable interface in a porous domain was considered in their paper. The porous medium was firstly saturated by the displaced fluid and was being infiltrated by the displacing fluid. Non-Newtonian shear-thinning power-law behavior was assumed to maintain continuous pressure and velocity at

the interface with constant initial pressure. Coupling the nonlinear flow law for both fluids, with the continuity equation, and taking into account compressibility effects, yielded a set of nonlinear second-order partial differential equations. Their transformation via a self-similar variable was done by considering the same flow behavior index for both the displacing and displaced fluids. A following transformation of the equations including the conditions at the interface has showed for pseudoplastic fluids the existence of a compression front ahead of the moving interface. Solving the resulting set of nonlinear equations yielded the moving interface position, the compression front position, and the pressure distributions which were derived in closed forms for all kinds of flow behavior. Federico and Ciriello stated that their solution could be used for complex numerical models, allowed to investigate the key processes and dimensionless parameters involved in non-Newtonian displacement in porous media, and extended the analytical approach and results of another different paper of them [8] on flow of a single power-law fluid to motion of two fluids, taking compressibility effects into account.

WU et al. [6] presented an analytical Buckley-Leverett-type [31] solution for one-dimensional immiscible displacement of a Newtonian fluid by a non-Newtonian fluid in porous media. They assumed the viscosity of the non-Newtonian fluid as a function of the flow potential gradient and the non-Newtonian phase saturation. Where, they developed a practical procedure for applying their method to field problems which is based on the analytical solution, similar to the graphic technique of Welge [32]. Their solution could be regarded as an extension of the Buckley-Leverett method to Non-Newtonian fluids. The results obtained by their analytical analysis revealed how the saturation profile and the displacement efficiency could be controlled by the relative permeabilities and by the inherent complexities of the non-Newtonian fluid. A couple examples of the application for their analytical solution were submitted in that research study. The

first one is the effect analysis of non-Newtonian behavior on immiscible displacement of a Newtonian fluid by a power-law non-Newtonian fluid. The second one is a verification of the numerical model for simulation of flow of immiscible non-Newtonian and the Newtonian fluids in porous media. Good agreement between the analytical and the numerical results was shown.

For complicated displacements of fluid in porous media, according to Walsh et al [43], the easiest way to understand it is through fractional flow theory, which is an application of a subset of the method of characteristics (MOC). Walsh et al extended the fractional flow theory understanding to the displacement of oil by a miscible solvent in the presence of an immiscible aqueous phase. The fractional flow theory was generalized by Pope [44], starting with the Buckley-Leverett theory for waterflooding, his mathematics have been based on the MOC. Pope also treated three-phase flow problems, which occurs in a variety of the EOR processes. While Rossen et al. [44] extended fractional flow methods for two-phase flow to non-Newtonian fluids in a cylindrical one-dimensional flow. They also analyzed the characteristic equations for the polymer applications and foam floods applications.

For composites infiltration related studies, the infiltration process is governed by the phenomena of fluid flow, capillarity, and the mechanics of potential preform deformation. These phenomena are governed by four basic parameters: viscosity of the liquid melt phase, the pressure dependent melt saturation in the preform, the preform permeability and porosity, and the preform stress strain behavior. Comparing these parameters, in particular of surface tension and viscosity values, across all matrix material classes indicated clear differences, explaining the main differences in the engineering practice from a composite matrix to another. However, the governing laws are the same [20].

Michaud et al. [20] reviewed the phenomena and the governing laws for the case of isothermal infiltration of a porous preform by a Newtonian fluid without a phase transformation, and four basic functional quantities were addressed. They presented some examples of model methodologies and compared them with the available experimental data. They also illustrated the applications of these governing laws using the analytical and numerical methods.

In another paper Michaud et al. [56] analyzed the infiltration by a pure matrix considering preform deformation and partial matrix solidification and studied the superheat influence within the infiltration metal, neglecting the pressure drop in the remelted region. They concluded that the superheat had only a minor effect on the infiltration kinetics, which is the same result of a rigid preform case, but the superheat significantly affected the remelted region length. Another conclusion of their work was that using a bounding approach, the upper bound, which ignored the solid metal influence on the preform relaxation, and lower bound, which assumed that the solid metal conferred complete rigidity to the preform, were close compared to other factors of uncertainty in the infiltration prediction. Finally, they concluded that neglecting the solid phase velocity for the liquid velocity and considering the melt superheat to be zero could bound the infiltration rate to become relatively simple to be calculated with good precision

In a study related to the manufacturing of metal matrix composites (MMCs), Lacoste et al. [39] pointed out the analogous numerical studies of the Resin Transfer Moulding (RTM) process and listed some technological difficulties which has encountered this process, in particular due to the appearance of many complex phenomena during processing. That analysis has included deformation of the fibrous preform, phase change of metal, and microporosities. They also presented some examples regarding the limits and possibilities offered by the numerical modelling.

In addition, they pointed out to some conditions that must be satisfied. As for the quality of the numerical simulation, they said it depends on the relevance of the used physical parameters.

Jung et al. [40] developed an axisymmetric finite element (FE) model for the process of squeeze casting the MMCs. They have numerically studied the flow in the mold, the infiltration into the porous preform, and the solidification of the molten metal. They used a simple preform deformation model to predict the permeability change caused by preform compression during infiltration. In addition, they did a series of infiltration experiments to validate the assumptions used in the numerical model. The comparison between the experimental and numerical data showed that the developed FE program successfully predicts the actual squeeze casting process. Jung et al. concluded that the higher the preheat temperature of the metal and the mold, the lower the infiltration pressure required, and the lower metal pressure results in less preform deformation.

For the properties of CMCs, which are usually manufactured by infiltration, Prielipp et al. [41] described the mechanical properties of metal reinforced ceramics, especially AI/A1203 composites with interpenetrating networks. Fracture strength and fracture toughness data were given as functions of two variables; ligament diameter and fiber volume fraction. Then, they compared their results with the corresponding values of the porous preforms. They also presented a simple model for accounting the influence of metal volume and metal ligament diameter on the composites' toughness. Their results showed that the increase in fracture strength from the porous preform to the composite is much larger than the increase of the fracture toughness increase alone, and the fracture strength of that material is increased more by metal infiltration than the plateau toughness derived from long crack measurements.

Jin [42] described a thermo-poroelasticity theory to investigate the effects of temperature gradients on the infiltration kinetics, pore pressure distribution of the liquid phase, and liquid

content variation due to preform deformation for infiltration processing of interpenetrating phase composites. He also derived a similarity solution for one-dimensional infiltration assuming no solidification of the liquid phase and showed that the infiltration front also depends on the poroelastic properties of the preform. A numerical example for a polymer–ceramic interpenetrating phase composite was presented and the results showed that the temperature gradients may produce significant liquid content increment beyond the amount that can be accommodated by the initial pore volume of the preform. This increment in liquid content may compensate some solidification shrinkage of the liquid phase and alter thermal residual stresses, thereby reducing occurrence of microdefects in the composite.

As reviewed above, flows of non-Newtonian fluids in porous media have been studied extensively. However, only Newtonian fluid has been used in the study of infiltration processing of composite materials (Jin [42], Michaud et al. [20], Jung et al. [40], Ouahbi et al. [22], Ambrosi [46] and Larsson et al. [47]. In the infiltration processing of composites, the fluid phase is a molten polymer or metal. Many polymers, however, are non-Newtonian fluids in the molten state [48,49,50]. Therefore, non-Newtonian fluid models should be used to better understand the melt flow behavior and solid preform deformation in the study of infiltration processing of composite materials. In addition, the infiltration front has been a major concern in the infiltration processing of composite materials. The objective of this thesis is to study infiltration processing of interpenetrating composites using a non-Newtonian fluid model. Both one-dimensional linear and radial flow of a non-Newtonian fluid in a porous preform will be studied. Equations to determine the non-dimensional isothermal infiltration front as a function of the known inlet boundary condition, i.e., inlet pressure or inlet fluid flux factor, are derived, and numerical examples are presented. Besides isothermal infiltration of a porous preform by a non-Newtonian fluid, non-

isothermal infiltration by a Newtonian fluid with convection heat transfer (which was ignored in [42]) is also studied numerically.

The organization of this thesis is as follows:

The first chapter introduces non-Newtonian fluid flow in porous media and reviews the previous work in this area with applications in petroleum engineering, chemical engineering and composite manufacturing.

In chapter 2, the isothermal linear infiltration of a porous solid by a non-Newtonian fluid is presented and the basic equations of 3-dimensional poroelasticiy are presented in the first section of this chapter. Then, the equations are reduced to one-dimensional flow in the second section. A self-similarity solution for a specified inlet pressure boundary condition and a numerical example, for a ceramic porous preform and a melted polymer, are presented in the third section of this chapter. While a self-similarity solution for a specified inlet flow rate boundary condition and a numerical example, with material parameters consistent with those of the third section, are presented in the fourth section of the chapter.

In chapter 3, the isothermal radial infiltration of a porous solid by a non-Newtonian fluid is presented and the basic equations of 3-dimensional poroelasticiy are presented in the first section of this chapter. Then, the equations are reduced to one-dimensional flow in the second section. A self-similarity solution for a specified inlet pressure boundary condition and a numerical example, for data consistent with the data of linear flow application, are presented in the third section of this chapter. While in the fourth section, a self-similarity solution for a specified inlet flow rate boundary condition and a numerical example, for data consistent with the data of linear flow application, are presented.

In chapter 4, the non-isothermal linear infiltration of a porous solid by a Newtonian fluid is presented, basic equations of 3-dimensional thermo-poroelasticiy are presented in the first section. Then, they are reduced to one-dimensional flow in the second section. A self-similarity solution for a specified inlet pressure boundary condition and a numerical example with convection heat transfer are presented in the third section of that chapter.

The fifth chapter incorporates the conclusions which could be obtained from the presented work.

2 ISOTHERMAL LINEAR FLOW OF A NON-NEWTONIAN FLUID IN A POROUS MEDIUM

2.1 Basic Equations of Poroelasticity

Fluid transport in the interstitial space in a porous solid can be described by the well-known Darcy's law which is an empirical equation for seepage flow in non-deformable porous media. It can also be derived from Navier-Stokes equations by dropping the inertial terms. Consistent with the current small deformation assumptions and by ignoring the fluid density variation effect (Hubert's Potential) [51]. Modified Darcy's law for non-Newtonian flow can be adopted here

$$q_i = -\kappa(p_{,i} - f_i)^{\frac{1}{n}}, \tag{1}$$

In the above equation, q_i is the specific discharge vector, or fluid flux vector, which describes the motion of the fluid relative to the solid and is formally defined as the rate of fluid volume crossing a unit area of porous solid whose normal is in the x_i direction, $f_i = \rho_f g_i$ the body force per unit volume of fluid (with ρ_f the fluid density, and g_i the gravity component in the i-direction), p the pore pressure, and $\kappa = k/\mu_{eff}$ the permeability coefficient or mobility coefficient (with k the intrinsic permeability having dimension of length squared, and μ_{eff} the effective viscosity of the fluid).

The following conventions have been adopted in writing the basic equations: a comma followed by subscripts denotes differentiation with respect to spatial coordinates and repeated indices in the same monomial imply summation over the range of the indices (generally x, y and z, unless otherwise indicated).

The effective viscosity of the fluid is given by Ref. [30]

$$\frac{k}{\mu_{eff}} = \frac{1}{2H}\left(\frac{n\phi_0}{3n+1}\right)^n \left(\frac{8k}{\phi_0}\right)^{(1+n)/2}, \tag{2}$$

where H is the consistency index, n the flow behavior index with $n < 1, = 1$, or > 1 describing respectively pseudoplastic, Newtonian, or dilatant behavior, and ϕ_0 the porosity. The porosity is assumed to be a constant like in the classical small deformation poroelasticity [42].

Two "strain" quantities are also introduced to describe the deformation and the change of fluid content of the porous solid with respect to an initial state: the usual small strain tensor ε_{ij} and the variation of fluid content ζ, defined as the variation of fluid volume per unit volume of porous material: ε_{ij} is positive for extension, while a positive ζ corresponds to a "gain" of fluid by the porous solid [51]. The strain tensor is related to the original kinematic variables u_i, the solid displacement vector that tracks the movement of the porous solid with respect to a reference configuration according to the following strain-displacement relations

$$\varepsilon_{ij} = \frac{1}{2}\left(u_{i,j} + u_{j,i}\right). \tag{3}$$

The fluid flux vector and the variation of fluid content satisfy the following continuity equation

$$\frac{\partial \zeta}{\partial t} = -q_{i,i}\,, \tag{4}$$

where t is the time.

For flow of an incompressible fluid, the fluid content variation is solely due to the deformation of the porous preform [42].

The stress and strain follow the constitutive equations in the framework of Biot theory [42]

$$\sigma_{ij} + \alpha p \delta_{ij} = 2G\varepsilon_{ij} + \frac{2G\upsilon}{1-2\upsilon}\varepsilon_{kk}\delta_{ij}\,, \tag{5}$$

$$2G\zeta = \frac{\alpha(1-2\upsilon)}{1+\upsilon}\left(\sigma_{kk} + \frac{3}{B}p\right), \tag{6}$$

where σ_{ij} is the total stress tensor, α identified as the Biot–Willis coefficient, G the shear modulus of the drained elastic solid, υ the drained Poisson's ratio, B the Skempton's coefficient, and δ_{ij} the Kronecker delta.

Finally, the following equilibrium equations supplement the basic governing equations of poroelasticity [42]

$$\sigma_{ij,j} = -F_i\,, \tag{7}$$

where $F_i = \rho g_i$ is the body force per unit volume of the bulk material.

2.2 Basic Equations for One-Dimensional Flow

In this section, we consider one-dimensional (1-D) isothermal infiltration of a porous solid by a non-Newtonian fluid in the x-direction as schematically shown in Figure 1. At a given moment of infiltration, the porous preform is divided into two regions, i.e., Region 1 in which the preform is infiltrated by the fluid, and Region 2 in which the preform has not yet been infiltrated. The two regions are separated by the moving infiltration front. In applications, infiltration can occur with three kinds of known boundary conditions. In the first case, which is termed the $p_0 - p_f$ problem, infiltration is driven by a specified fluid pressure at the inlet, $x = 0$, and the pressure

at the infiltration front is also given. In the second case, which is termed the $Q_0 - p_f$ problem, the fluid flow in the porous preform is caused by a specified flow rate at the inlet, $x = 0$, with the pore pressure specified at the other end. Finally, the third case in which the flow rates are specified at both ends and is termed the $Q_0 - Q_f$ problem [30]. The first 2 cases will be discussed in this thesis.

In the 1-D problems, we assume that no lateral deformation and fluid flow occur, which corresponds to infiltration of the preform confined by a rigid and impermeable mold. Moreover, the body force is not considered. Hence, the following strain and fluid flux components are zero

$$\varepsilon_{yy} = \varepsilon_{zz} = \varepsilon_{xy} = \varepsilon_{yz} = \varepsilon_{xy} = u_y = u_z = 0, \tag{8a}$$

$$q_y = q_z = 0. \tag{8b}$$

Moreover, all field variables are functions of x and time t, for example, the pore pressure field is $p = p(x, t)$. Under the above 1-D isothermal infiltration assumptions, the constitutive equations in (01), (4), (5), (6) and (7) reduce to

$$q_x = \left(-\frac{k}{\mu_{eff}} \frac{\partial p}{\partial x} \right)^{\frac{1}{n}}, \tag{9}$$

$$\frac{\partial \zeta}{\partial t} + \frac{\partial q_x}{\partial x} = 0, \tag{10}$$

$$\sigma_{xx} = 2G \frac{1 - \nu}{1 - 2\nu} \varepsilon_{xx} - \alpha\, p, \tag{11}$$

$$\zeta = \alpha \varepsilon_{xx} + \left(-\frac{\alpha^2}{K} + \frac{\alpha}{KB} \right) p, \tag{12}$$

$$\frac{\partial \sigma_{xx}}{\partial x} = 0, \tag{13}$$

where K is the drained Bulk modulus.

Designated boundary conditions at the inlet, $x = 0$, are either constant pressure p_0 or flow rate $Q_w(t)$

$$p = p_0, x = 0, \tag{14a}$$

or

$$q_x = \frac{Q_w(t)}{A}, x = 0, \tag{14b}$$

where A is the cross section area of the porous preform, and

$$Q_w(t) = Q_0 t^c, \tag{15}$$

where Q_0 is the injection intensity and c a real number.

The boundary condition at the infiltration front is

$$p = p_f = 0, x = x_f\ , \tag{16}$$

where x_f is the infiltration front, and will be determined later.

Lastly, the stress σ_{xx} at the inlet is known to be

$$\sigma_{xx} = -p_0, x = 0. \tag{17}$$

The above boundary conditions need to be supplemented by the continuity of stress σ_{xx} and displacement u_x at the infiltration front. It follows from the equilibrium equation (13) that the stress σ_{xx} is a constant which is determined by the boundary condition (17) as $-p_0$. We thus have the following normal stress along the infiltration direction

$$\sigma_{xx} = -p_0, 0 \le x \le x_f\ . \tag{18}$$

Substituting Eq. (18) into (11) yields the strain as follows:

$$\varepsilon_{xx} = \frac{1-2\nu}{2G(1-\nu)}(\alpha\, p - p_0) = \frac{(1+\nu)}{3K(1-\nu)}(\alpha\, p - p_0). \tag{19}$$

Substituting the above into Eq. (12), we get the variation of fluid content

$$\zeta = \left(\frac{-2+4\nu}{3(1-\nu)}\alpha^2 + \frac{\alpha}{B}\right)\frac{p}{K} - \frac{(1+\nu)}{3K(1-\nu)}\alpha p_0 = \tilde{S}\frac{p}{K} - \frac{\alpha}{3K}\frac{1+\nu}{1-\nu}p_0\,, \tag{20}$$

where $\tilde{S}$ is a dimensionless constant given by

$$\tilde{S} = \frac{\alpha}{B} - \frac{2(1-2\nu)}{3(1-\nu)}\alpha^2. \tag{21}$$

Substituting equations (9) and (20) into Eq. (10), we obtain the following nonlinear, partial differential equation for the pore pressure

$$\frac{\tilde{S}}{K}\frac{\partial p}{\partial t} - \frac{1}{n}\left(\frac{k}{\mu_{eff}}\right)^{\frac{1}{n}}\left(-\frac{\partial p}{\partial x}\right)^{\frac{1-n}{n}}\frac{\partial^2 p}{\partial x^2} = 0. \tag{22}$$

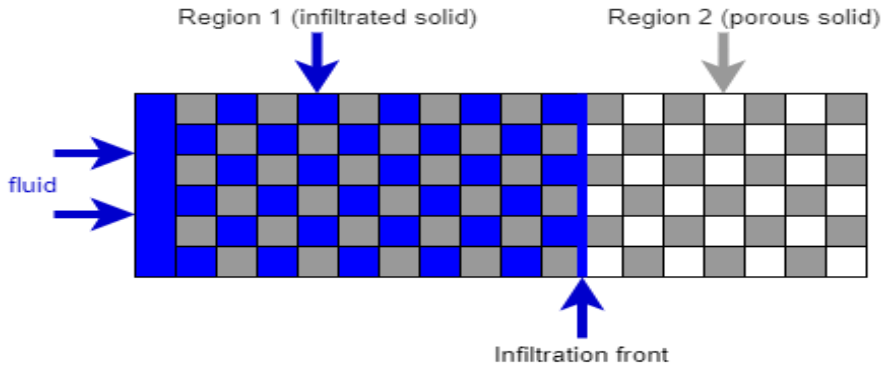

Figure 1 Schematic of linear infiltration of a porous preform by a fluid

2.3 The $p_0 - p_f$ Problem

2.3.1 A Self-Similarity Solution

Following [42], we seek a similarity solution for the problem. Introduce a dimensionless distance η as follows:

$$\eta = x\left(\frac{k}{\mu_{eff}}K\right)^{\frac{-1}{n+1}} t^{\frac{-n}{n+1}}, \tag{23}$$

In the similarity solution, the pore pressure has the following form

$$p(x,t) = p_0\tilde{p}(\eta), \tag{24}$$

where $\tilde{p}$ is a dimensionless pore pressure and is a function of η only.

The basic equation (22) and the boundary conditions for the pore pressure now become

$$\frac{d^2\tilde{p}}{d\eta^2} - \frac{n^2}{n+1}\left(\frac{p_0}{K}\right)^{\frac{n-1}{n}} \tilde{S}\eta\left(-\frac{d\tilde{p}}{d\eta}\right)^{\frac{2n-1}{n}} = 0, \tag{25}$$

$$\tilde{p} = 1, \eta = 0, \tag{26}$$

$$\tilde{p} = 0, \eta = \eta_f\ , \tag{27}$$

where η_f is a constant and related to the infiltration front x_f by

$$\eta_f = x_f\left(\frac{k}{\mu_{eff}}K\right)^{\frac{-1}{n+1}} t^{\frac{-n}{n+1}}. \tag{28}$$

Integrating Eq. (25) yields

$$\frac{d\tilde{p}}{d\eta} = -\left[C_1 - \frac{n(1-n)}{2(n+1)}\left(\frac{p_0}{K}\right)^{\frac{n-1}{n}}\tilde{S}\eta^2\right]^{\frac{n}{1-n}}, \tag{29}$$

where C_1 is an integration constant.

The solution of Eq. (29) under the boundary conditions (26) is

$$\tilde{p}(\eta) = 1 - \int_0^{\eta}\left[C_1 - \frac{n(1-n)}{2(n+1)}\left(\frac{p_0}{K}\right)^{\frac{n-1}{n}}\tilde{S}\eta^2\right]^{\frac{n}{1-n}} d\eta. \tag{30}$$

Using the boundary condition (27) in (30), we obtain the following equation satisfied by the integration constant C_1

$$1 - \int_0^{\eta_f}\left[C_1 - \frac{n(1-n)}{2(n+1)}\left(\frac{p_0}{K}\right)^{\frac{n-1}{n}}\tilde{S}\eta^2\right]^{\frac{n}{1-n}} d\eta = 0. \tag{31}$$

The constant C_1 can be expressed in terms of η_f and p_0 by the condition

$$\frac{dx_f}{dt} = \frac{1}{\phi_0} q_x|_{x=x_f}, \tag{32}$$

i.e., the velocity of the infiltration front is the fluid flux at the front divided by the porosity ϕ_0 [42].

$$C_1 = \eta_f^{1-n}\left(\frac{n+1}{n\phi_0}\right)^{n-1}\left(\frac{p_0}{K}\right)^{\frac{n-1}{n}} + \frac{n(1-n)}{2(n+1)}\left(\frac{p_0}{K}\right)^{\frac{n-1}{n}}\tilde{S}\eta_f^2. \tag{33}$$

Substituting C_1 in Eq. (33) into Eq. (31), we obtain

$$\int_0^{\eta_f} \left[\eta_f^{1-n} \left(\frac{n+1}{n\phi_0} \right)^{n-1} + \frac{n(1-n)}{2(n+1)} \tilde{S}\left(\eta_f^2 - \eta^2\right) \right]^{\frac{n}{1-n}} d\eta - \frac{p_0}{K} = 0. \tag{34}$$

The above is the equation to determine the non-dimensional infiltration front η_f as a function of the applied initial pressure p_0.

2.3.2 Numerical Results and Discussion

This section presents numerical examples of the non-dimensional infiltration front η_f versus the applied inlet pressure p_0, the dimensional infiltration front x_f as a function of time t, the normalized pore pressure $\tilde{p}$ along the infiltration direction η, and the normalized liquid content variation $\zeta/(p_0/K)$ along the infiltration direction η. Table 1 lists the poroelastic parameters for the fluid-filled porous medium in the numerical calculations [42]. The liquid phase is a molten polymer and the preform is a ceramic material for possible dental applications. The viscosity value is chosen to be $0.1\ Pa.s$, which is the viscosity for Epoxy during infiltration [20]. Molten polymers have a viscosity range from $0.1\ Pa.s$ (for typical uncured thermoset matrices) to $10^4\ Pa.s$ (for thermoplastic polymers) [20]. The results are shown for 2 values of flow behavior index, $n = 0.5$ and $n = 0.8$. The flow behavior index of commercial polymers varies between 0.2 and 0.8 [57].

The infiltration front is the most important quantity in the infiltration processing of composite materials [42]. Figure 2 shows, for $n = 0.5$, the non-dimensional infiltration front η_f versus the applied fluid pressure p_0, with various values of the preform porosity. While Figure 3 shows the results for $n = 0.8$. It is shown, as expected, that the non-dimensional infiltration front

η_f increases with an increase in the applied pressure p_0. Comparing the results in Figure 2 and Figure 3, it is clear that dimensionless infiltration front also increases with the increase of the flow behavior index n.

Table 1 Poroelastic parameters for the fluid-filled porous medium

Bulk modulus (drained) $[GPa]$	K=10
Poisson's ratio (drained)	$\upsilon = 0.25$
Permeability $[mD]$	$\kappa = 100$
Biot–Willis coefficient	$\alpha = 0.8$
Skempton's coefficient	$B = 0.6$
Preform porosity	$\phi_0 = 0.1, 0.3, 0.5$
Flow behavior index	$n = 0.5, 0.8$
Fluid consistency index $[Pa\ s^n]$	$H = 0.1$

Figure 4 shows, for $n = 0.5$, the dimensional infiltration front x_f as a function of time t, the dimensional infiltration front x_f is given in equation (23), i.e., $x_f = \eta_f \left(\frac{k}{\mu_{eff}} K\right)^{\frac{1}{n+1}} t^{\frac{n}{n+1}}$, under an applied pressure of $p_0 = 10\ MPa$. The dimensionless infiltration front values, for $n = 0.5$, are $\eta_f = 3.11 \times 10^{-2}, 2.15 \times 10^{-2}$, and 1.82×10^{-2} for $\phi_0 = 0.1$, 0.3, and 0.5, respectively, other parameters are listed in Table 1. While Figure 5 shows the results for $n = 0.8$, under the same

applied pressure. The dimensionless infiltration frontvalues, for $n = 0.8$, are $\eta_f = 8.59 \times 10^{-2}, 5.27 \times 10^{-2}$, and 4.2×10^{-2} for $\phi_0 = 0.1$, 0.3, and 0.5, respectively, other parameters are the same as those in Figure 4. As expected, it is shown that the infiltration front increases with time.

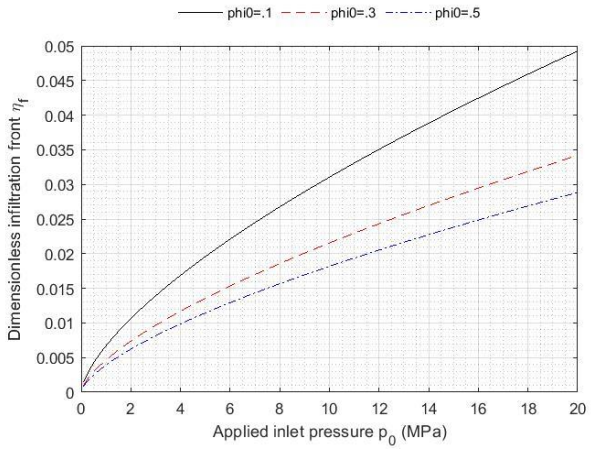

Figure 2 Dimensionless Infiltration front versus the applied pressure for $n = 0.5$

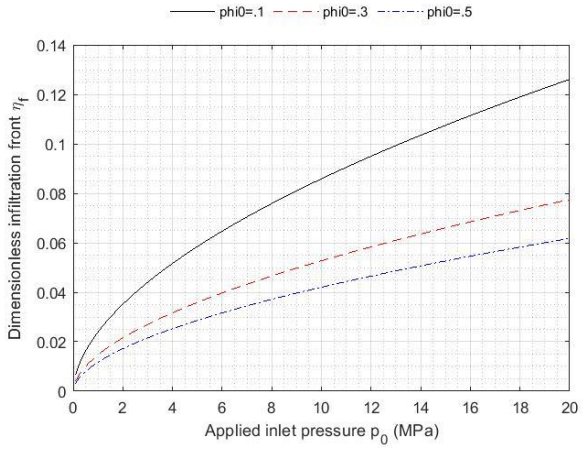

Figure 3 Dimensionless Infiltration front versus the applied pressure for $n = 0.8$

Figure 6 shows, for $n = 0.5$, the normalized pore pressure (p/p_0) of the percolating fluid along the infiltration direction. under an applied inlet pressure of $p_0 = 10\ MPa$. All parameters

and the non-dimensional infiltration front are the same as those in Figure 4. While Figure 7 shows the results for $n = 0.8$, under the same applied inlet pressure and for the same parameters, the non-dimensional infiltration front values are the same as those in Figure 5. It is shown that the normalized pore pressure decreases with the distance increasing from the inlet and drops to zero at the infiltration front, where the fluid stops moving. The pressure distribution is almost linear.

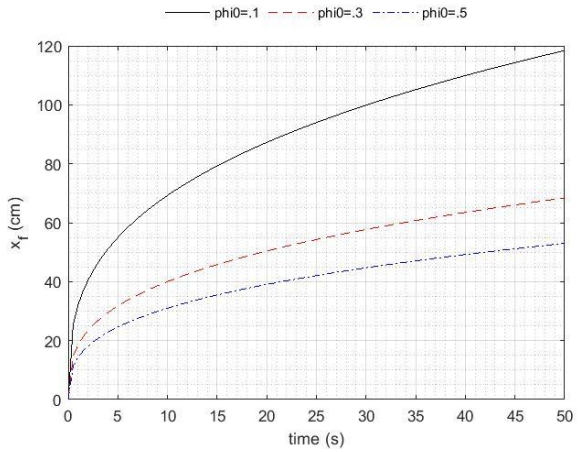

Figure 4 Dimensional infiltration front versus time for $n = 0.5$

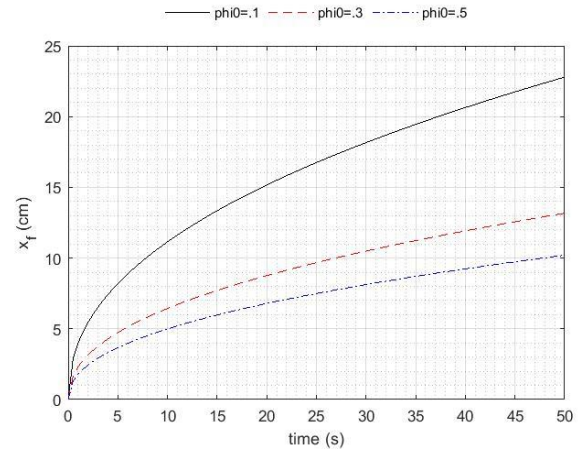

Figure 5 Dimensional infiltration front versus time for $n = 0.8$

Figure 8 shows, for $n = 0.5$, the normalized fluid content variation along the infiltration direction, under an applied inlet pressure of $p_0 = 10\ MPa$. All other parameters and the non-dimensional infiltration front are the same as those in Figure 4. While Figure 9 shows the results for $n = 0.8$, under the same applied pressure and for the same parameters with the non-dimensional infiltration front are the same as those in Figure 5. For a given porosity ϕ_0 of the preform, the fluid content variation is the highest at the inlet and remains positive until η reaches about 55% of the infiltration front and becomes negative from there to the infiltration front. This can be explained, mathematically, by looking at Eq. (20) and noting that there is a negative constant term, $-\frac{\alpha}{3K}\frac{1+\nu}{1-\nu}p_w$, which remains constant, and negative, along the infiltration direction, and there is a positive term, $\tilde{S}\frac{p}{K}$, which is, by looking at Figure 8 and Figure 9, the highest at the inlet and vanishes at the interface. Another explanation for the negative fluid content variation is that the increment in fluid content may offset some solidification shrinkage of the liquid phase, thereby reducing occurrence of microdefects caused by solidification shrinkage [42].

A problem of special interest is the prediction of the flow-rate decline in time at the inlet, i.e. at $x = 0$ [30]. Since the pressure distribution is known from substituting the value of c_1 in Eq. (33) into Eq. (29) then the modified Darcy's law (9) allows the knowledge of the flow rate variation expressed in terms of the dimensionless distance η and time t. This variation may be written as

$$q_{x|x=0} = \left(-\frac{k}{\mu_{eff}}\frac{\partial p}{\partial x}\right)^{\frac{1}{n}} = \left(-\frac{k}{\mu_{eff}}p_0\frac{d\tilde{p}}{d\eta}\left(\frac{k}{\mu_{eff}}K\right)^{-\frac{1}{n+1}}\right)^{\frac{1}{n}} t^{\frac{-1}{n+1}}. \tag{35}$$

The above equation indicates that the flow rate at the inlet is a power function of time.

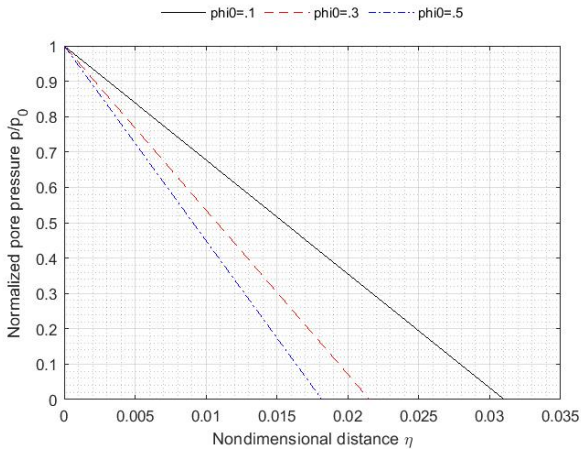

Figure 6 Normalized pore pressure along the infiltration direction for $n = 0.5$

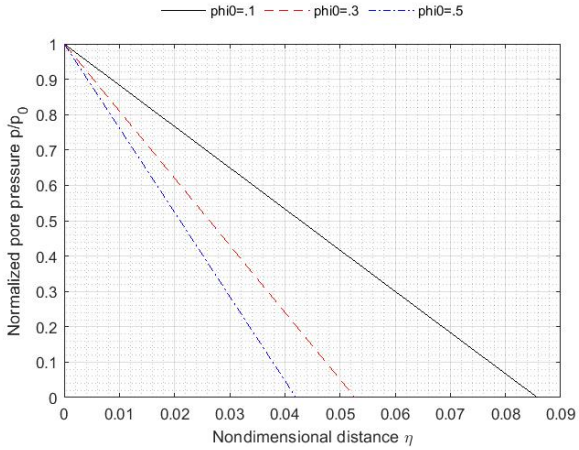

Figure 7 Normalized pore pressure along the infiltration direction for $n = 0.8$

2.4 The $Q_0 - p_f$ Problem

In practice, instead of a constant pressure of production at the inlet, a variable flow rate $Q_0 t^c$, may also be given at the inlet to drive the fluid flow in the porous media. In this case, knowledge of pressure variation in time at the outface flow is of great practical interest. As field observations have shown, the flow rate at the outface flow declines as a continuous monotonic

function of time [30]. On the other hand, Eq. (35) indicates that, for a constant pressure at $x = 0$, the flow rate decline is expressed by the relation

$$Q(0,t) = Q_0 t^{\frac{-1}{n+1}}, \tag{36}$$

where Q_0 is the injection intensity. In general, in self-similar infiltration of a porous solid, the flow rate at the inlet is a function of time, instead of a constant.

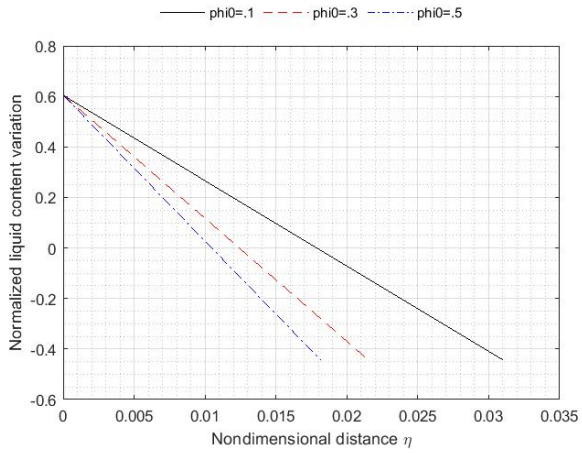

Figure 8 Normalized fluid content variation along the infiltration direction for $n = 0.5$

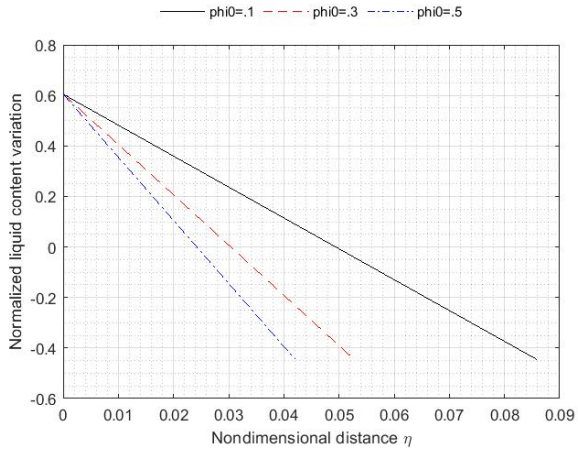

Figure 9 Normalized fluid content variation along the infiltration direction for $n = 0.8$

Now, we have the following differential equation, Eq. (22), for the pore pressure

$$\frac{\tilde{S}}{K}\frac{\partial p}{\partial t} - \frac{1}{n}\left(\frac{k}{\mu_{eff}}\right)^{\frac{1}{n}}\left(-\frac{\partial p}{\partial x}\right)^{\frac{1-n}{n}}\frac{\partial^2 p}{\partial x^2} = 0, \tag{37}$$

and the boundary conditions

$$q_x = \frac{Q_w(t)}{A}, x = 0, \tag{38}$$

$$p = 0, x = x_f\ , \tag{39}$$

where

$$Q_w = Q_0 t^{\frac{-1}{n+1}}. \tag{40}$$

2.4.1 A Self-Similarity Solution

We, again, seek a similarity solution for the problem. Introduce a dimensionless distance η as follows:

$$\eta = x\left(\frac{k}{\mu_{eff}}K\right)^{\frac{-1}{n+1}} t^{\frac{-n}{n+1}}. \tag{41}$$

In the similarity solution, the pore pressure has the following form:

$$p(x,t) = EQ_w\tilde{p}(\eta), \tag{42}$$

where $E\ [ML^{-4}T^{-1}]$ is a constant, and $\tilde{p}$ a non-dimensional pore pressure and is a function of η only.

Using the dimensionless variables, the basic equation (37) and the boundary conditions for the pore pressure now become

$$\frac{d^2\tilde{p}}{d\eta^2} - \left(\frac{EQ_w}{K}\right)^{\frac{n-1}{n}} \frac{n^2}{n+1} \tilde{S}\eta \left(-\frac{d\tilde{p}}{d\eta}\right)^{\frac{2n-1}{n}} = 0, \tag{43}$$

$$q_x = \frac{Q_w(t)}{A}, \eta = 0, \tag{44}$$

$$\tilde{p} = 0, \eta = \eta_f \, . \tag{45}$$

Integrating Eq. (43), we get

$$\frac{d\tilde{p}}{d\eta} = -\left[C_2 - \frac{n(1-n)}{2(n+1)}\left(\frac{EQ_w}{K}\right)^{\frac{n-1}{n}} \tilde{S}\eta^2\right]^{\frac{n}{1-n}}, \tag{46}$$

where C_2 is an integration constant. Using the following infiltration front condition

$$\frac{dx_f}{dt} = \frac{1}{\phi_0} q_x|_{x=x_f} \, . \tag{47}$$

the constant C_2 can be determined as follows:

$$C_2 = \eta_f^{1-n}\left(\frac{n+1}{n\phi_0}\right)^{n-1}\left(\frac{EQ_w}{K}\right)^{\frac{n-1}{n}} + \frac{n(1-n)}{2(n+1)}\left(\frac{EQ_w}{K}\right)^{\frac{n-1}{n}} \tilde{S}\eta_f^2 \, . \tag{48}$$

Substituting C_2 in Eq. (48) into Eq. (4648), we obtain

$$\frac{d\tilde{p}}{d\eta} = -\left[\eta_f^{1-n}\left(\frac{n+1}{n\phi_0}\right)^{n-1}\left(\frac{EQ_w}{K}\right)^{\frac{n-1}{n}} + \frac{n(1-n)}{2(n+1)}\left(\frac{EQ_w}{K}\right)^{\frac{n-1}{n}}\tilde{S}\eta_f^2 - \frac{n(1-n)}{2(n+1)}\left(\frac{EQ_w}{K}\right)^{\frac{n-1}{n}}\tilde{S}\eta^2\right]^{\frac{n}{1-n}}. \quad (49)$$

Using the boundary condition (44) and Eqs. (36), (49) and (9), we obtain the following equation

$$\frac{Q_0}{A} = \left[\left(\frac{k}{\mu_{eff}}\right)^{\frac{n}{n+1}} K^{\frac{-1}{n+1}}\left(\eta_f^{1-n}\left(\frac{n+1}{n\phi_0}\right)^{n-1} K^{\frac{1-n}{n}} + \frac{n(1-n)}{2(n+1)}K^{\frac{1-n}{n}}\tilde{S}\eta_f^2\right)^{\frac{n}{1-n}}\right]^{\frac{1}{n}}. \quad (50)$$

The above equation is used to determine the non-dimensional infiltration front η_f in terms of the flow-rate factor Q_0.

2.4.2 Numerical Results and Discussion

This section presents numerical examples of the non-dimensional infiltration front η_f versus the inlet flux factor Q_0, and the dimensional infiltration front x_f as a function of time t. The infiltration front is the most important quantity in the infiltration processing. The front in the similarity solution is represented by the dimensionless parameter η_f.

Figure 10 shows, for $n = 0.5$, the non-dimensional infiltration front η_f versus the inlet flux factor Q_0, with various values of the preform porosity, for the parameters listed in Table 1, and a well cross section area of $A = 5\ cm^2$. While Figure 11 shows the results for $n = 0.8$ for the same parameters. As expected, the figures show that the infiltration front increases with the inlet flux

factor, Q_0, increasing. By comparing the two figures, the nondimensional infiltration front η_f increases with an increase in the flow behavior index n.

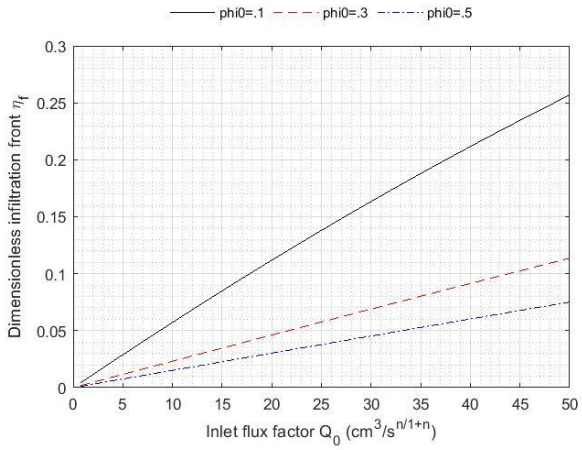

Figure 10 Dimensionless Infiltration front versus the inlet flux factor for $n = 0.5$

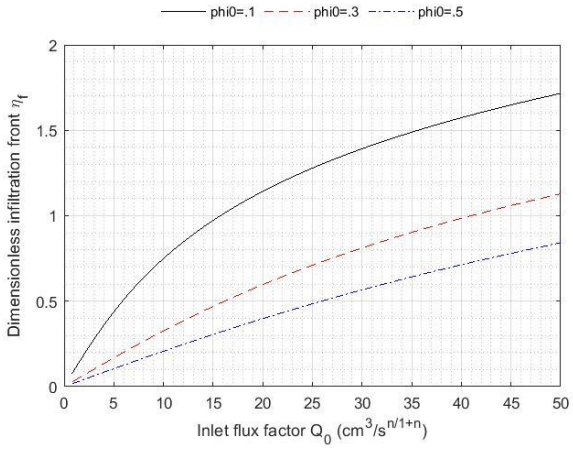

Figure 11 Dimensionless Infiltration front versus the inlet flux factor for $n = 0.8$

Figure 12 shows, for $n = 0.5$, the dimensional infiltration front x_f as a function of time t, the dimensional infiltration front x_f is given in equation (23), i.e., $x_f = \eta_f \left(\frac{k}{\mu_{eff}} K\right)^{\frac{1}{n+1}} t^{\frac{n}{n+1}}$, under an inlet flux factor of $8\ cm^3/s^{.5/1.5}$. the dimensionless infiltration front values are $\eta_f =$

$0.046, 0.019$ and 0.012 for $\phi_0 = 0.1,\ 0.3$, and 0.5, respectively, other parameters are listed in Table 1. While Figure 13 shows the results for $n = 0.8$ under an inlet flux factor of $Q_0 = 8\ cm^3/s^{.8/1.8}$, for the same applied pressure and same parameters, the dimensionless infiltration front are $\eta_f = 0.638, 0.265$ and 0.167 for $\phi_0 = 0.1, 0.3$, and 0.5, respectively. As expected, it is shown that the dimensional infiltration front increases with time.

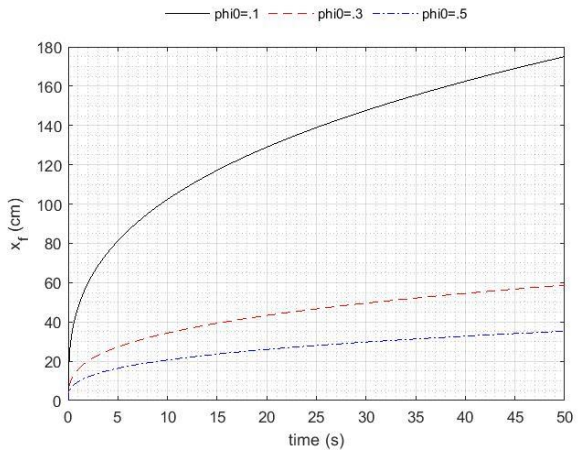

Figure 12 Dimensional infiltration front versus time for $n = 0.5$

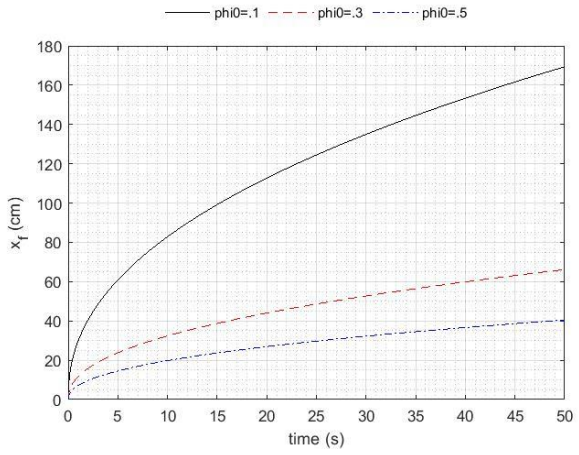

Figure 13 Dimensional infiltration front versus time for $n = 0.8$

3 ISOTHERMAL RADIAL FLOW OF A NON-NEWTONIAN FLUID IN A POROUS MEDIUM

3.1 Basic Equations of Radial Flow

In infiltration processing of hollow composite cylinders, the fluid flows in the radial direction. This chapter thus considers infiltration of a porous preform by a non-Newtonian fluid in the radial direction. We consider an infinite porous medium with a hole of a constant thickness h and a radius r_w located in the center of a porous domain, as schematically shown in Figure 14, and analyze the moving infiltration front and the pore pressure of the fluid along the infiltration direction, due to injection at the hole of a non-Newtonian fluid into the porous solid. The fluid is injected at a constant pressure p_w, or at a given injection rate $Q_w(t)$.

The flow in the interconnected pores of the porous preform follows the modified Darcy's law

$$q_r = \left(-\frac{k}{\mu_{eff}} \frac{\partial p}{\partial r} \right)^{\frac{1}{n}}, \tag{51}$$

where r denotes the radial spatial coordinate.

The continuity equation is given by [38]

$$\frac{\partial q_r}{\partial r} + \frac{q_r}{r} = -c_0 \phi_0 \frac{\partial p}{\partial t}, \tag{52}$$

where $c_0 = c_f + c_p$ is the total compressibility coefficient in the flow region, with c_f being the fluid compressibility coefficient and c_p the porous medium compressibility coefficient. The above continuity equation does not exactly follow that in poroelasticity. It is an approximation more

commonly used in applications that implicitly assumes that the pore pressure is proportional to the fluid content variation.

Substituting Eq. (51) in Eq. (52) one obtains

$$\frac{1}{n}\left(-\frac{k}{\mu_{eff}}\frac{\partial p}{\partial r}\right)^{\frac{1-n}{n}}\left(\frac{k}{\mu_{eff}}\frac{\partial^2 p}{\partial r^2}\right)-\frac{1}{r}\left(-\frac{k}{\mu_{eff}}\frac{\partial p}{\partial r}\right)^{\frac{1}{n}}=c_0\phi_0\frac{\partial p}{\partial t}. \tag{53}$$

For the boundary condition at the hole, we have two cases. The first case corresponds to a constant applied inlet pressure, while the second relates to a variable flow rate of production

$$p=p_w, r=r_w\,, \tag{54a}$$

or

$$q_r=\frac{Q_w(t)}{2\pi h r_w}, r=r_w\,, \tag{54b}$$

where r_w is the hole radius, h hole thickness, and

$$Q_w(t)=Q_o t^c, \tag{55}$$

in which c is a constant to be determined.

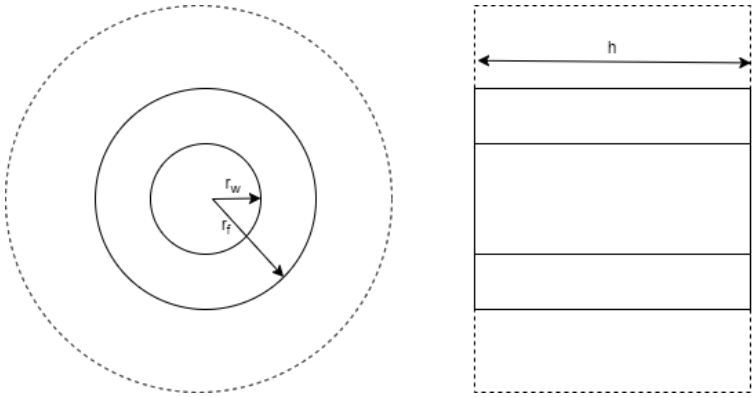

Figure 14 Schematic of radial infiltration of a porous preform by a fluid

The boundary condition at the infiltration front in both cases is

$$p = p_f = 0,\ r = r_f\ , \tag{56}$$

where r_f is the radius of the infiltration front.

3.2 The $p_0 - p_f$ Problem

3.2.1 A Self-Similarity Solution

We, again, seek a similarity solution for the problem. Introduce a dimensionless distance η as follows:

$$\eta = r\left(\frac{k}{\mu_{eff}}\frac{1}{c_0}\right)^{\frac{-1}{n+1}} t^{\frac{-n}{n+1}}, \tag{57}$$

In the similarity solution, the pore pressure has the following form:

$$p = p_w\tilde{p}(\eta). \tag{58}$$

The basic equation (53) and the boundary conditions for the pore pressure now become

$$\frac{\eta}{n}\left(-\frac{d\tilde{p}}{d\eta}\right)^{\frac{1-n}{n}}\left(\frac{d^2\tilde{p}}{d\eta^2}\right) - \left(-\frac{d\tilde{p}}{d\eta}\right)^{\frac{1}{n}} = -\frac{n}{n+1}c_0{}^{\frac{n-1}{n}}\phi_0 p_w{}^{\frac{n-1}{n}}\eta^2\frac{d\tilde{p}}{d\eta}, \tag{59}$$

$$\tilde{p} = 1, \eta = \eta_w\ , \tag{60}$$

$$\tilde{p} = 0, \eta = \eta_f\ , \tag{61}$$

where η_w is a time variable and η_f a constants, and related respectively to the well radius r_w and infiltration front r_f by

$$\eta_w = r_w \left(\frac{k}{\mu_{eff}} \frac{1}{c_0} \right)^{\frac{-1}{n+1}} t^{\frac{-n}{n+1}}, \tag{62}$$

$$\eta_f = r_f \left(\frac{k}{\mu_{eff}} \frac{1}{c_0} \right)^{\frac{-1}{n+1}} t^{\frac{-n}{n+1}}. \tag{63}$$

Integrating Eq. (59) yields

$$\frac{d\tilde{p}}{d\eta} = -\eta^{-n} \left(\frac{n^2 - n}{(3-n)(1+n)} {c_0}^{\frac{n-1}{n}} \phi_0 {p_w}^{\frac{n-1}{n}} \eta^{3-n} + C \right)^{\frac{n}{1-n}}, \tag{64}$$

where C is an integration constant, which can be expressed in terms of η_f and p_w by the infiltration front condition

$$\frac{dr_f}{dt} = \frac{1}{\phi_0} q_r|_{r=r_f}, \tag{65}$$

$$C = N^{1-n} {\eta_f}^{2(1-n)} - M {\eta_f}^{3-n}, \tag{66}$$

where M and N are dimensionless constants and related to the injected pressure p_w by

$$M = \frac{n^2 - n}{(3-n)(1+n)} {c_0}^{\frac{n-1}{n}} \phi_0 {p_w}^{\frac{n-1}{n}}, \tag{67}$$

$$N = \frac{n}{n+1} {c_0}^{\frac{-1}{n}} \phi_0 {p_w}^{\frac{-1}{n}}, \tag{68}$$

Now Eq. (64) becomes

$$\frac{d\tilde{p}}{d\eta} = -\eta^{-n}\left(M\eta^{3-n} - M{\eta_f}^{3-n} + N^{1-n}{\eta_f}^{2(1-n)}\right)^{\frac{n}{1-n}}. \tag{69}$$

The solution of Eq. (69) under the boundary conditions (60) is

$$\tilde{p} = 1 - \int_{\eta_w}^{\eta} \eta^{-n}\left(M\eta^{3-n} - M{\eta_f}^{3-n} + N^{1-n}{\eta_f}^{2(1-n)}\right)^{\frac{n}{1-n}} d\eta. \tag{70}$$

We may approximate $\eta_w \cong 0$, since $\eta_w << \eta$ [38]. In this case, eq (70) becomes

$$\tilde{p} = 1 - \int_{0}^{\eta} \eta^{-n}\left(M\eta^{3-n} - M{\eta_f}^{3-n} + N^{1-n}{\eta_f}^{2(1-n)}\right)^{\frac{n}{1-n}} d\eta. \tag{71}$$

Using the boundary condition (61), we obtain

$$\int_{0}^{\eta_f} \eta^{-n}\left(M\eta^{3-n} - M{\eta_f}^{3-n} + N^{1-n}{\eta_f}^{2(1-n)}\right)^{\frac{n}{1-n}} d\eta - 1 = 0. \tag{72}$$

The above is the equation to determine the non-dimensional infiltration front η_f as a function of the applied initial pressure p_w.

3.2.2 Numerical Results and Discussion

This section presents numerical examples of the non-dimensional infiltration front η_f versus the applied inlet pressure p_w, the dimensional infiltration front r_f as a function of time t, and the pore pressure $\tilde{p}$ along the infiltration direction η. Table 2 lists the poroelastic parameters for the fluid-filled porous medium in our numerical study, which are consistent with the parameters of the linear flow problem mentioned in the previous chapter.

Table 2 Poroelastic parameters for the fluid-filled porous medium

Total compressibility coefficient $[Pa^{-1}]$	$c_0 = 1 \times 10^{-10}$
Preform porosity	$\phi_0 = 0.1, 0.3, 0.5$
Permeability $[mD]$	$\kappa = 100$
Flow behavior index	$n = 0.5, 0.8$
Fluid consistency index $[Pa\ s^n]$	$H = 0.1$

The infiltration front is the most important quantity in the infiltration processing [42]. Figure 15 shows, for $n = 0.5$, the non-dimensional infiltration front η_f versus the applied inlet fluid pressure p_w with various values of the preform porosity. While Figure 16 shows the results for $n = 0.8$. It is shown that the non-dimensional infiltration front η_f increases with an increase in the applied inlet fluid pressure p_w. Comparing the results in the two figures, it is clear that dimensionless infiltration front increases with the increase in the flow behavior index n.

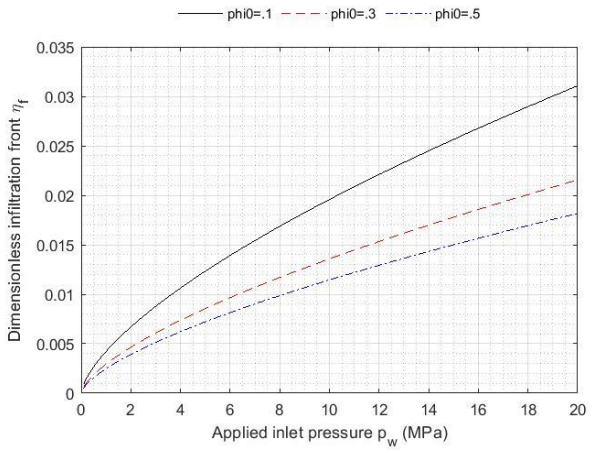

Figure 15 Dimensionless infiltration front versus applied pressure for $n = 0.5$

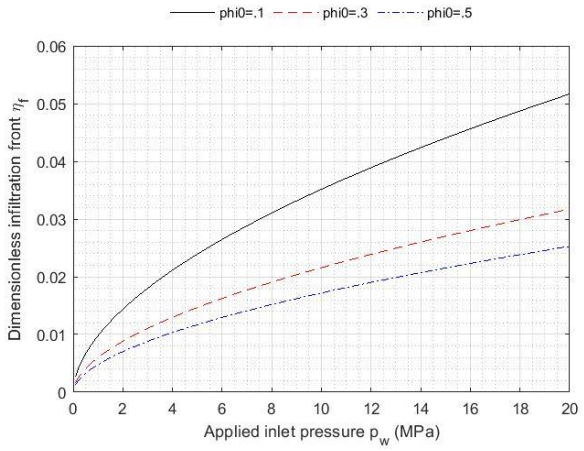

Figure 16 Dimensionless infiltration front versus applied pressure for $n = 0.8$

Figure 17 shows, for $n = 0.5$, the dimensional infiltration front r_f as a function of time t, the dimensional infiltration front r_f is given in equation (57), i.e., $r_f = \eta_f \left(\frac{k}{\mu_{eff}} \frac{1}{c_0}\right)^{\frac{1}{n+1}} t^{\frac{n}{n+1}}$, under an applied pressure of $p_w = 10\, MPa$. The dimensionless infiltration front values are $\eta_f = 1.96 \times 10^{-2}, 1.36 \times 10^{-2}$, and 1.14×10^{-2} for $\phi_0 = 0.1, 0.3$, and 0.5, respectively, other parameters are listed in Table 2. While Figure 18 shows the results for $n = 0.8$, under the same applied pressure and for the same parameters. The dimensionless infiltration front values are $\eta_f = 3{,}52 \times 10^{-2}, 2.16 \times 10^{-2}$, and 1.72×10^{-2} for $\phi_0 = 0.1, 0.3$, and 0.5, respectively. As expected, it is shown that the infiltration front increases with time.

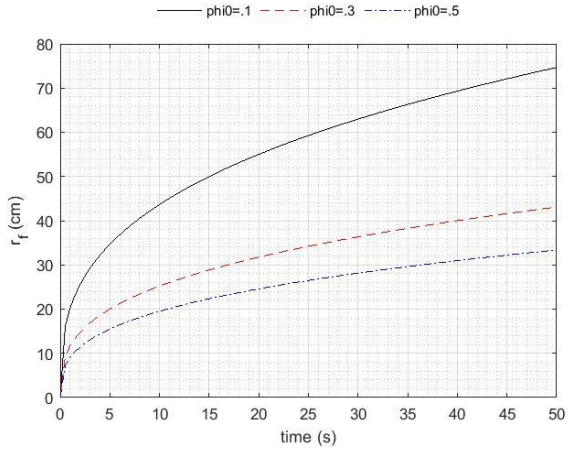

Figure 17 Dimensional infiltration front versus time for $n = 0.5$

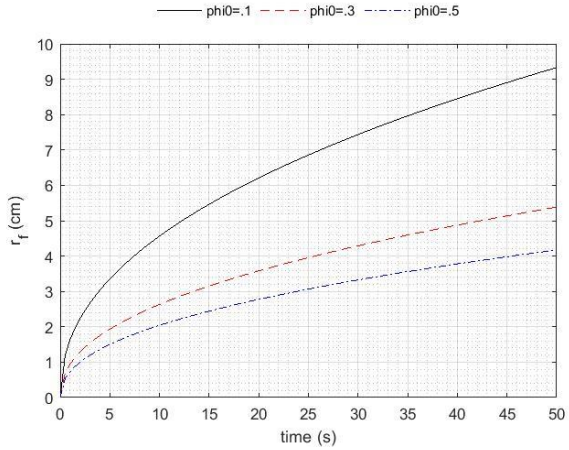

Figure 18 Dimensional infiltration front versus time for $n = 0.8$

Figure 19 shows, for $n = 0.5$, the normalized pore pressure (p/p_0) of the percolating fluid along the infiltration direction. under an applied inlet pressure of $p_w = 10\ MPa$. All parameters and the non-dimensional infiltration front are the same as those in Figure 17. While Figure 20 shows the results for $n = 0.8$, for the same parameters, and the nondimensional infiltration front values in Figure 18. It is shown that the normalized pore pressure decreases with the distance

increasing from the inlet and drops to zero at the infiltration front, where the fluid stops moving. The pressure distribution is not linear.

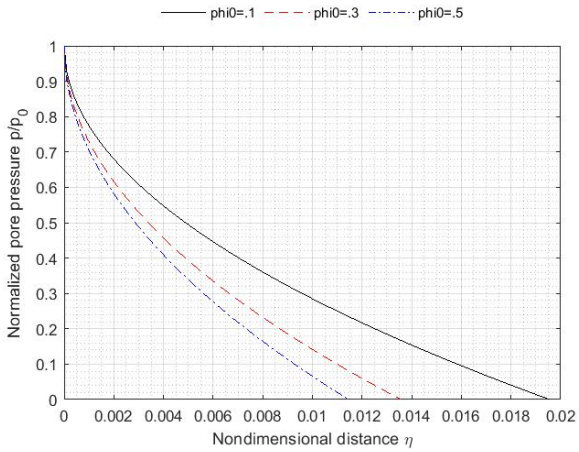

Figure 19 Normalized pore pressure along the infiltration direction for $n = 0.5$

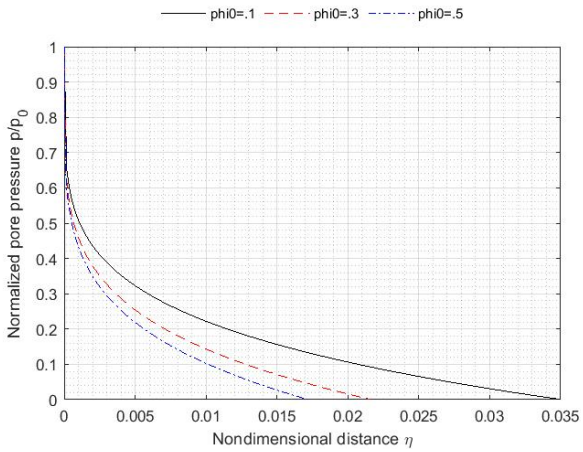

Figure 20Normalized pore pressure along the infiltration direction for $n = 0.8$

3.3 The $Q_0 - p_f$ Problem

As mentioned in the previous chapter, instead of a constant pressure of production at the hole, a variable flow rate, $Q_0 t^c$, may also be given at the inlet to drive the porous fluid flow. The constant c is given by Ref. [38] and Ref. [30]

$$c = \frac{n-1}{n+1}. \tag{73}$$

So, the flow rate at the hole is expressed by the relation

$$Q(r_w, t) = Q_o t^{\frac{n-1}{n+1}}, \tag{74}$$

where Q_o is the injection intensity.

Now, we have the following differential equation, Eq (53), for the pore pressure

$$\frac{1}{n}\left(-\frac{k}{\mu_{eff}}\frac{\partial p}{\partial r}\right)^{\frac{1-n}{n}}\left(\frac{k}{\mu_{eff}}\frac{\partial^2 p}{\partial r^2}\right) - \frac{1}{r}\left(-\frac{k}{\mu_{eff}}\frac{\partial p}{\partial r}\right)^{\frac{1}{n}} = c_0\phi_0\frac{\partial p}{\partial t}, \tag{75}$$

and the following boundary conditions

$$q_r = \frac{Q_w(t)}{2\pi h r_w}, r = r_w\,, \tag{76}$$

$$p = p_f = 0, r = r_f\,, \tag{77}$$

where

$$Q_w = Q_o t^{\frac{n-1}{n+1}}. \tag{78}$$

3.3.1 A Self-Similarity Solution

We, again, seek a similarity solution for the problem. Introduce a dimensionless distance η as follows:

$$\eta = r\left(\frac{k}{\mu_{eff}}\frac{1}{c_0}\right)^{\frac{-1}{n+1}} t^{\frac{-n}{n+1}}. \tag{79}$$

In the similarity solution, the pore pressure has the following form:

$$p(x,t) = DQ_w\tilde{p}(\eta), \tag{80}$$

where D $[ML^{-4}T^{-1}]$ is a constant, and $\tilde{p}$ is the nondimensional pore pressure and is a function of η only.

Using the dimensionless variables, the basic equation (75) and the boundary conditions for the pore pressure now become

$$\frac{\eta}{n}\left(-\frac{d\tilde{p}}{d\eta}\right)^{\frac{1-n}{n}}\left(\frac{d^2\tilde{p}}{d\eta^2}\right) - \left(-\frac{d\tilde{p}}{d\eta}\right)^{\frac{1}{n}} = -\frac{n}{n+1}c_0^{\frac{n-1}{n}}\phi_0(DQ_w)^{\frac{n-1}{n}}\eta^2\frac{d\tilde{p}}{d\eta}, \tag{81}$$

$$q_r = \frac{Q_w(t)}{2\pi h r_w}, \eta = \eta_w\,, \tag{82}$$

$$\tilde{p} = 0, \eta = \eta_f\,. \tag{83}$$

Integrating Eq. (81), we get

$$\frac{d\tilde{p}}{d\eta} = -\eta^{-n}\left(\frac{n^2-n}{(3-n)(1+n)}c_0^{\frac{n-1}{n}}\phi_0(DQ_w)^{\frac{n-1}{n}}\eta^{3-n} + C_0\right)^{\frac{n}{1-n}}, \tag{84}$$

where C_0 is an integration constant. Using the infiltration front condition

$$\frac{dr_f}{dt} = \frac{1}{\phi_0} q_r|_{r=r_f}, \tag{85}$$

the constant C_0 can be determined as follows:

$$C_0 = \left(V^{1-n}{\eta_f}^{2(1-n)} - W{\eta_f}^{3-n}\right)(DQ_w)^{\frac{n-1}{n}}, \tag{86}$$

where W and V are constants given by

$$W = \frac{n^2 - n}{(3-n)(1+n)} {c_0}^{\frac{n-1}{n}} \phi_0, \tag{87}$$

$$V = \frac{n}{n+1} {c_0}^{\frac{-1}{n}} \phi_0. \tag{88}$$

Now Eq. (84) becomes

$$\frac{d\tilde{p}}{d\eta} = -\eta^{-n}\left(W\eta^{3-n} - W{\eta_f}^{3-n} + V^{1-n}{\eta_f}^{2(1-n)}\right)^{\frac{n}{1-n}}(DQ_w)^{-1}. \tag{89}$$

Using the boundary condition (82), and Eqs. (74), (89) and (51), we obtain the following equation

$$\frac{Q_o}{2\pi h} = \left(\frac{k}{\mu_{eff}}\right)^{\frac{2}{n+1}} {c_0}^{\frac{1-n}{n^2+n}}\left(W{\eta_w}^{3-n} - W{\eta_f}^{3-n} + V^{1-n}{\eta_f}^{2(1-n)}\right)^{\frac{1}{1-n}}. \tag{90}$$

Since the well radius r_w is very small, $\eta_w << \eta$, we may approximate $\eta_w \cong 0$. In this case, Eq. (90) becomes

$$\frac{Q_o}{2\pi h} = \left(\frac{k}{\mu_{eff}}\right)^{\frac{2}{n+1}} {c_0}^{\frac{1-n}{n^2+n}}\left(-W{\eta_f}^{3-n} + V^{1-n}{\eta_f}^{2(1-n)}\right)^{\frac{1}{1-n}}. \tag{91}$$

The above equation is used to determine the non-dimensional infiltration front η_f in terms of the flow-rate factor Q_o

3.3.2 Numerical Results and Discussion

This section presents numerical examples of the non-dimensional infiltration front η_f versus the inlet flux factor Q_o, and the dimensional infiltration front r_f as a function of time t. Table 2 lists the poroelastic parameters for the fluid-filled porous medium in our numerical calculations.

As mentioned earlier, the infiltration front is the most important quantity in the infiltration processing. The front in the similarity solution is represented by the dimensionless parameter η_f . Figure 21 shows, for $n = 0.5$, the non-dimensional infiltration front η_f versus the inlet flux factor Q_o, with various values of the preform porosity, for the parameters listed in Table 2, and a hole thickness of $h = 5\ mm$. While Figure 22 shows the results for $n = 0.8$ for the same parameters. As expected, the figures show that the infiltration front increases with the inlet flux factor Q_o increase. By comparing Figure 21 and Figure 22, the nondimensional infiltration front η_f increases with an increase in the flow behavior index n.

Figure 23 shows, for $n = 0.5$, the dimensional infiltration front r_f as a function of time t, the dimensional infiltration front r_f is given in equation (57), i.e., $r_f = \eta_f \left(\frac{k}{\mu_{eff}} \frac{1}{c_0}\right)^{\frac{1}{n+1}} t^{\frac{n}{n+1}}$, under an inlet flux factor of $Q_o = 8\ cm^3/s^{.5/1.5}$. the dimensionless infiltration front values are $\eta_f = 8.4 \times 10^{-3}, 5.9 \times 10^{-3}$, and 4.9×10^{-3} for $\phi_0 = 0.1$, 0.3, and 0.5, respectively, other parameters are the same as those in Figure 21. While Figure 24 shows the results for $n = 0.8$ under the same inlet flux factor, and the same parameters. The dimensionless infiltration front values are $\eta_f =$

$0.162, 0.1,$ and 0.079 for $\phi_0 = 0.1, 0.3,$ and 0.5, respectively. As expected, it is shown that the infiltration front increases with time.

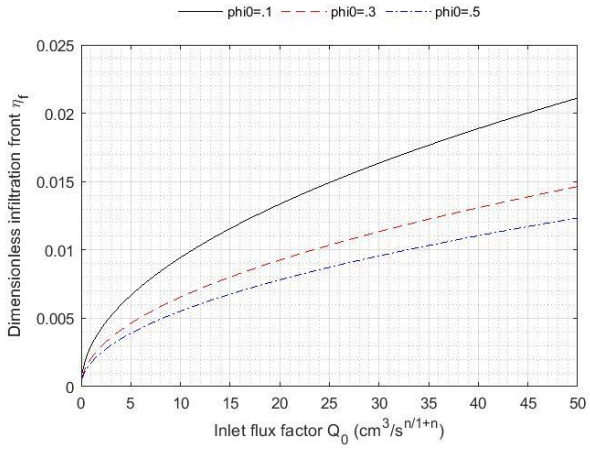

Figure 21 Dimensionless Infiltration front versus the inlet flux factor for $n = 0.5$

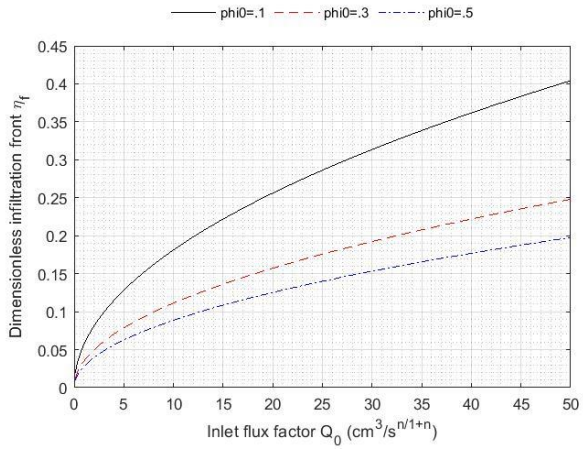

Figure 22 Dimensionless Infiltration front versus the inlet flux factor for $n = 0.8$

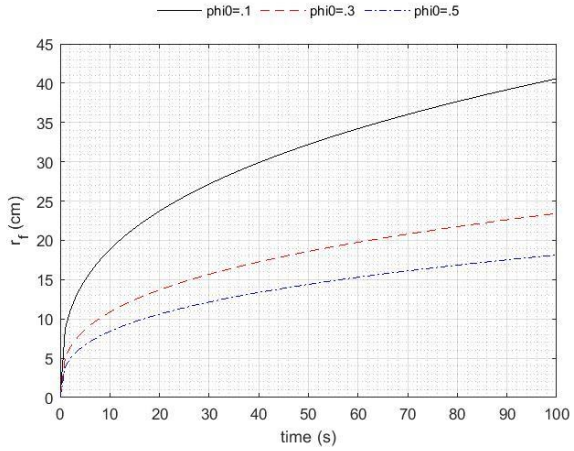

Figure 23 Dimensional infiltration front versus time for $n = 0.5$

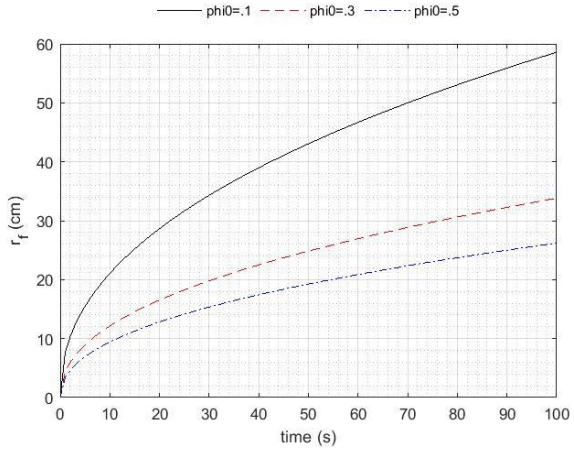

Figure 24 Dimensional infiltration front versus time for $n = 0.8$

4 NON-ISOTHERMAL LINEAR FLOW OF A NEWTONIAN FLUID IN A POROUS MEDIUM

4.1 Basic Equations of Thermo-Poroelasticity

Following the theoretical framework described in [42], the flow system to be analyzed in this chapter is a non-isothermal porous solid infiltrated by a Newtonian fluid with applications in the infiltration processing of composite materials. It is assumed that the porous preform and the liquid phase have different temperatures and no solidification of the liquid phase occurs during infiltration. As schematically shown in Figure 25, at a given moment of infiltration, the porous preform is divided into two regions. The infiltrated region is called Region 1, and the region that has not yet been infiltrated is Region 2. While the interface separates the two regions.

Clearly, Region 1 is a fluid-filled porous medium. The fluid moves in the interconnected pores of the preform, which is subjected to the applied mechanical loads, temperature variation, and pore fluid pressure. Fluid flow in the porous preform is described by Darcy's law

$$q_i = -\frac{k}{\mu_{eff}} p_{,i} \,, \tag{92}$$

For Newtonian fluid ($n = 1$), which is considered in this Chapter, the effective viscosity μ_{eff} in equation (20) reduces to conventional viscosity μ [38].

The continuity equation for fluid flow is given by

$$\frac{\partial \zeta}{\partial t} = -q_{i,i} \,, \tag{93}$$

Next, by looking at the heat transfer model in Region 1, the Fourier's law for heat conduction is

$$h_i = -\lambda_1 \theta_{,i} \,, \tag{94}$$

where h_i is the heat flux vector, θ is the temperature variation, and λ_1 is the thermal conductivity of the fluid-filled porous medium in Region 1. The temperature is governed by the heat conduction equation

$$\rho_1 c_1 \frac{\partial \theta}{\partial t} = \lambda_1 \nabla^2 \theta + q_{fs} \,, \tag{95}$$

where ρ_1 and c_1 are the mass density and specific heat of the fluid-filled porous medium in Region-1, respectively, ∇^2 the Laplacian operator. and q_{fs} accounts for the convection induced heat transfer and is given by

$$q_{fs} = -\rho_f c_f q_i \theta_{,i} \,, \tag{96}$$

where ρ_f and c_f are the mass density and specific heat of the fluid, respectively.

Substituting equation (96) into equation (95), we get

$$\rho_1 c_1 \frac{\partial \theta}{\partial t} + \rho_f c_f q_i \theta_{,i} = \lambda_1 \nabla^2 \theta. \tag{97}$$

In thermo-poroelasticity, the constitutive equations are [52]

$$\sigma_{ij} = 2G\varepsilon_{ij} + \frac{2G\upsilon}{1-2\upsilon}\varepsilon_{kk}\delta_{ij} - \alpha p \delta_{ij} - K\alpha_s \theta \delta_{ij} \,, \tag{98}$$

$$\zeta = \frac{\alpha}{3K}\left(\sigma_{kk} + \frac{3p}{B}\right) - \phi_0(\alpha_f - \alpha_s)\theta, \tag{99}$$

where α_s is the volumetric thermal expansion coefficient of the preform, and α_f the volumetric thermal expansion coefficient of the fluid.

Finally, the strains, displacements, and stresses satisfy the following strain–displacement relations and equations of equilibrium:

$$\varepsilon_{ij} = \frac{1}{2}\left(u_{i,j} + u_{j,i}\right). \tag{100}$$

$$\sigma_{ij,j} = 0. \tag{101}$$

Region 2 is the porous preform. The basic equations are the standard heat conduction and thermoelasticity equations [53].

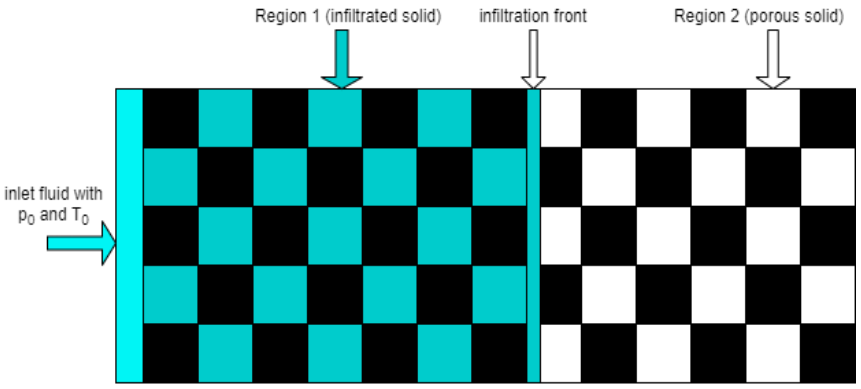

Figure 25 Schematic of non-isothermal linear infiltration of a porous preform by a fluid

4.2 Basic Equations for One-Dimensional Flow

This thesis is concerned with one-dimensional (1-D) infiltration in the x-direction as schematically shown in Figure 25. It is also assumed no deformation or fluid flow occur in the other two directions. Hence,

$$u_y = u_z = 0, \tag{102a}$$

$$\varepsilon_{yy} = \varepsilon_{zz} = \varepsilon_{xy} = \varepsilon_{yz} = \varepsilon_{xy} = 0, \tag{102b}$$

$$q_y = q_z = 0. \tag{103}$$

Now all field variables are functions of x and time t, for example, the temperature variation is $\theta = \theta(x,t)$.

The boundary conditions for the problem are

$$p = p_0, x = 0, \tag{104}$$

$$p = 0,\ x = x_f\ , \tag{105}$$

$$\sigma_{xx} = -p_0, x = 0, \tag{106}$$

$$\theta = \theta_0, x = 0, \tag{107}$$

where θ_0 is the inlet temperature.

Now the equilibrium equation (101) reduces to Eq. (13) in Chapter 2, i.e.,

$$\sigma_{xx,x} = 0, \tag{108}$$

which means the normal stress σ_{xx} is a constant. Using the boundary condition (106), we get

$$\sigma_{xx} = -p_0, 0 \le x \le x_f\ . \tag{109}$$

4.2.1 Region 1 $(0 < x < x_f)$

Under the above 1-D isothermal infiltration conditions, Darcy's law reduces to

$$q_x = -\kappa \frac{\partial p}{\partial x}. \tag{110}$$

The normal stresses and strain for the 1D infiltration can be deduced from Eqs. (98), (102a) (102b) and the boundary condition (106) as follows:

$$\sigma_{yy} = \sigma_{zz} = -\frac{\upsilon}{1-\upsilon} p_0 - \frac{1-2\upsilon}{1-\upsilon}(\alpha p + K\alpha_s \theta_1), \tag{111}$$

$$\varepsilon_{xx} = \frac{1+\upsilon}{3(1-\upsilon)K}(-p_0 + \alpha p K \alpha_s \theta_1) \tag{112}$$

where θ_1 the temperature variation in Region 1. Now the governing equations for the temperature variation, pore pressure, and liquid content variation reduce to

$$\frac{\partial \theta_1}{\partial t} - \frac{\rho_f c_f}{\rho_1 c_1}\kappa \frac{\partial p}{\partial x}\frac{\partial \theta_1}{\partial x} - \kappa_1 \frac{\partial^2 \theta_1}{\partial x^2} = 0, \tag{113}$$

$$\frac{\partial p}{\partial t} = \kappa \frac{K}{\tilde{S}}\frac{\partial^2 p}{\partial x^2} + \frac{K\omega\alpha_s}{\tilde{S}}\frac{\partial \theta_1}{\partial t}, \tag{114}$$

$$\zeta = \frac{\tilde{S}}{K} p - \omega \alpha_2 \theta_1 - \frac{\alpha}{3K}\frac{1+\upsilon}{1-\upsilon} p_0 \,, \tag{115}$$

where ω is a dimensionless parameter given by

$$\omega = \frac{2(1-2\upsilon)}{3(1-\upsilon)}\alpha + \phi_0 \frac{\alpha_f - \alpha_s}{\alpha_s}, \tag{116}$$

and κ_1 is the thermal diffusivity of the porous preform, and given by the equation

$$\kappa_1 = \lambda_1/(\rho_1 c_1), \tag{117}$$

in which λ_1 is the thermal conductivity, ρ_1 the density, and c_1 the specific heat of the porous preform, respectively.

4.2.2 Region 2 $(x > x_f)$

Region 2 is the porous preform. The temperature variation field is governed by the standard heat equation, i.e.,

$$\frac{\partial \theta_2}{\partial t} = \kappa_2 \frac{\partial^2 \theta_2}{\partial x^2}, \tag{118}$$

where κ_2 is the thermal diffusivity of the porous preform

$$\kappa_2 = \lambda_2/(\rho_2 c_2), \tag{119}$$

where λ_2 is the thermal conductivity, ρ_2 the density, and c_2 the specific heat of the porous preform, respectively.

Boundary conditions for the temperature variation at the interface between Regions 1 and 2, i.e., the infiltration front, are deduced from the temperature and heat flux continuity conditions as follows:

$$\theta_1(x_f, t) = \theta_2(x_f, t), t > 0, \tag{120}$$

$$\lambda_1 \frac{\partial \theta_1}{\partial x}(x_f, t) = \lambda_2 \frac{\partial \theta_2}{\partial x}(x_f, t), t > 0. \tag{121}$$

The temperature θ_2 goes to the initial temperature of the preform at distances far from the infiltration front. We thus have the third boundary condition as follows:

$$\theta_2 \to 0, x \to \infty. \tag{122}$$

4.3 A Self-Similarity Solution

Again, we seek a similarity solution for the non-isothermal infiltration problem. Introduce a dimensionless distance η as follows:

$$\eta = x/\sqrt{\frac{k}{\mu}Kt}. \tag{123}$$

In the similarity solution, the pore pressure, temperature variation in Region1, and temperature variation in Region 2 have the following forms:

$$p(x,t) = p_0\tilde{p}(\eta). \tag{124}$$

$$\theta_1(x,t) = T_0\tilde{\theta}_1(\eta). \tag{125}$$

$$\theta_2(x,t) = T_0\tilde{\theta}_2(\eta). \tag{126}$$

Under the self-similar infiltration conditions, Eqs. (113) and (114) for Region 1 become [42]

$$\frac{d^2\tilde{\theta}_1}{d\eta^2} + \frac{1}{2\kappa_1}\frac{kK}{\mu}\eta\frac{d\tilde{\theta}_1}{d\eta} + \frac{\rho_f c_f p_0}{\lambda_1}\frac{k}{\mu}\frac{d\tilde{p}}{d\eta}\frac{d\tilde{\theta}_1}{d\eta} = 0. \tag{127}$$

$$\frac{d^2\tilde{p}}{d\eta^2} + \frac{1}{2}\tilde{S}\eta\frac{d\tilde{p}}{d\eta} - \frac{K\omega\alpha_s T_0}{2p_0}\eta\frac{d\tilde{\theta}_1}{d\eta} = 0. \tag{128}$$

Clearly the temperature and pore pressure in Region 1 are coupled together due to the convective heat transfer. Moreover, the equations are nonlinear. The convection term was neglected in the solution in [42]. The boundary conditions for the normalized temperature and pore pressure are

$$\tilde{\theta}_1(0) = \theta_0/T_0\,. \tag{129}$$

$$\tilde{\theta}_1(\eta_f) = \tilde{\theta}_2(\eta_f). \tag{130}$$

$$\lambda_1 \frac{d\tilde{\theta}_1}{d\eta}(\eta_f) = \lambda_2 \frac{d\tilde{\theta}_2}{d\eta}(\eta_f). \tag{131}$$

$$\tilde{p}(0) = 1. \tag{132}$$

$$\tilde{p}(\eta_f) = 0. \tag{133}$$

In Region 2, the governing equation for the temperature, Eq. (118), becomes

$$\frac{d^2\tilde{\theta}_2}{d\eta^2} + \frac{1}{2\kappa_2}\frac{kK}{\mu}\eta\frac{d\tilde{\theta}_2}{d\eta} = 0. \tag{134}$$

Integrating the above equation yields

$$\frac{d\tilde{\theta}_2}{d\eta} = D_1 e^{-\frac{1}{2\kappa_2}\frac{kK}{\mu}\frac{\eta^2}{2}}, \tag{135}$$

where $D_1 \neq D_1(\eta, \tilde{\theta}_2)$ is a constant to be determined. The solution of the above equation is

$$\tilde{\theta}_2 = D_1\sqrt{\frac{\pi\mu\kappa_2}{kK}}\left[\mathrm{erf}\left(\sqrt{\frac{kK}{\mu}}\frac{\eta}{2\sqrt{\kappa_2}}\right) - 1\right]. \tag{136}$$

Using the above temperature expressions in Region 2, the continuity conditions in Equations (130) and (131) become

$$\tilde{\theta}_1(\eta_f) = D_1\sqrt{\frac{\pi\mu\kappa_2}{kK}}\left[\operatorname{erf}\left(\sqrt{\frac{kK}{\mu}}\frac{\eta_f}{2\sqrt{\kappa_2}}\right) - 1\right], \tag{137}$$

$$\frac{d\tilde{\theta}_1}{d\eta}(\eta_f) = \frac{\lambda_2}{\lambda_1}D_1 e^{-\frac{1}{2\kappa_2}\frac{kK\eta_f^2}{\mu}}. \tag{138}$$

4.4 Numerical Results and Discussion

This section presents the numerical examples of the non-dimensional infiltration front η_f versus the applied inlet pressure p_0, the dimensional infiltration front x_f as a function of time t, the pore pressure $\tilde{p}$ along the infiltration direction η, the temperature distribution θ along the infiltration direction η, and the normalized liquid content variation $\zeta/(p_0/K)$ along the infiltration direction η during the infiltration of a ceramic preform by a liquid polymer with the same properties used in [42], which are possible for dental applications [42]. Table 1 lists the poroelastic parameters for the fluid-filled porous medium in the numerical calculations and Table 3 lists the thermal properties of the fluid and solid phases.

The specific heat capacity and density for the fluid-filled porous solid in Region 1 is determined using the following rule of mixtures [42]:

$$\rho_1 = \phi_0\rho_f + (1-\phi_0)\rho_s, \tag{139}$$

$$c_1 = \phi_0 c_f + (1-\phi_0)c_s, \tag{140}$$

subscripts f and s denote the properties of the fluid and solid phases, respectively, and the porosity is the volume fraction of the fluid phase. The thermal conductivity in Region 1 is determined using a matricity-based model for interpenetrating phase composites as follows [54]:

$$k_1 = k_{II} + \frac{(k_I - k_{II})M_\alpha}{(1-r) + r\left(M_\alpha + M_\beta\, k_I/k_{II}\right)}, \tag{141}$$

where k_I and k_{II} are the thermal conductivities of αM (solid as matrix) and βM (fluid as matrix) phases and are determined using the models of the Hashin-Shtrikman [55]

$$k_I = k_\alpha \left\{1 + \frac{(1-\phi_0)\left(k_\beta - k_\alpha\right)}{k_\alpha + \left(k_\beta - k_\alpha\right)\phi_0/3}\right\}, \tag{142}$$

$$k_{II} = k_\beta \left\{1 + \frac{(1-\phi_0)\left(k_\alpha - k_\beta\right)}{k_\beta + \left(k_\alpha - k_\beta\right)\phi_0/3}\right\}, \tag{143}$$

where k_α and k_β are the thermal conductivities of the α-phase (fluid) and β-phase (solid), respectively. The matricities M_α and M_β describe the connectivity of the α-phase (fluid) and β-phase (solid) in the fluid-filled preform, respectively. Because both the solid and fluid are fully interconnected, the matricities are taken as 0.5. Moreover, parameter r is also taken as 0.5 in the calculation as it does not significantly influence the thermal conductivity. While the same properties in Region 2 are determined by the same methods by taking the properties of the air, instead of the liquid, as the α- phase.

The nonlinear equations (127) and (128) are solved numerically using the Runge-Kutta 4th order method. To solve for $\eta_f(p_0)$, and $D_1(p_0)$, the unknowns in the boundary conditions, the 2 coupled differential equations with the 5 boundary conditions and the infiltration front velocity boundary condition, Eq. (32), are solved firstly at some specific points of p_0 using trial and error

method. $D_1(p_0)$ and $\eta_f(p_0)$ can then be estimated using the curve fitting method. After that, $D_1(p_0)$ and $\eta_f(p_0)$ can be solved using trial and error method with an accepted error, but with the search range of D_1 and the search range of η_f at every point being reduced to the range around the value gotten from the previous step.

Table 3 Thermal parameters for the fluid and solid phases

	Fluid	Solid
Density $[Kg/m^3]$	$\rho_f = 1000$	$\rho_s = 3000$
Specific heat $[J/(Kg\ K)]$	$c_f = 1200$	$c_s = 800$
Coefficient of thermal expansion (volumetric) $[1/K]$	$\alpha_f = 300 \times 10^{-6}$	$\alpha_f = 24 \times 10^{-6}$
Thermal conductivity $[w/(m\ K)]$	$k_{Tf} = 0.15$	$k_{Ts} = 20$

As mentioned above, The infiltration front is the most important quantity in infiltration processing of interpenetrating phase composites. The front in the similarity solution is represented by the dimensionless parameter η_f. Figure 26 shows the non-dimensional infiltration front η_f versus the applied inlet fluid pressure p_0 with an initial preform temperature of $T_0 = 500\ K$ and an inlet liquid temperature of $490\ K$ $(\theta_0 = -10\ K)$. It is seen that the infiltration front η_f increases with the applied inlet pressure p_0 for a given porosity. At a given inlet pressure, a smaller porosity of the preform yields a higher value of η_f indicating faster processing. By comparing the results to [42], where the convection term was ignored, it looks like the convection does not have an effect on the infiltration front.

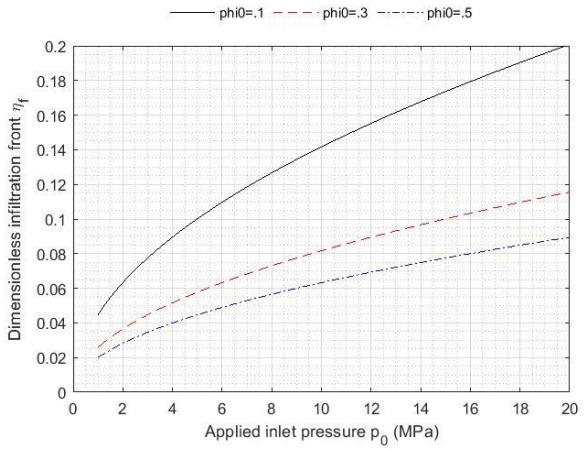

Figure 26 Dimensionless Infiltration front versus the applied pressure

Figure 27 shows the dimensional infiltration front x_f as a function of time t, the dimensional infiltration front is given by Eq. (123), i.e., $x_f = \eta_f \left(\frac{k}{\mu_{eff}} K\right)^{\frac{1}{2}} t^{\frac{1}{2}}$, under an applied pressure of $p_0 = 10\, MPa$. The dimensionless infiltration front for values are $\eta_f = 6.32 \times 10^{-2}, 8.17 \times 10^{-2}$, and 0.142 for $\phi_0 = 0.1, 0.3$, and 0.5, respectively. Other parameters are the same as those in Table 1 and Table 3. As shown the infiltration front increases with the time increasing.

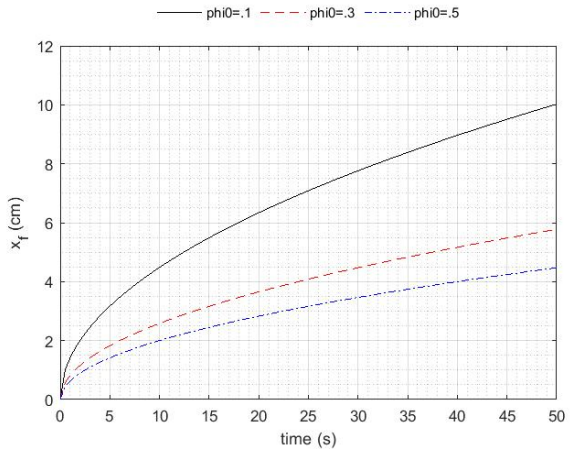

Figure 27 Dimensional infiltration front along the time

Figure 28 shows the temperature variation distribution θ, θ_1 along the infiltration direction in region 1 $(0 \leq \eta \leq \eta_f)$, (black, red, and blue lines), and θ_2 along the infiltration direction in region 2 $(\eta \geq \eta_f)$, (green, cyan, and magenta lines), the two lines are connected at the interface through the continuity condition equation (130), under an applied pressure of $p_0 = 10\,MPa$ for various values of the preform porosity. The dimensionless infiltration front values are the same as those in Figure 27 and other parameters are the same as those in Figure 26. Note that the temperature variation at the inlet is $10\,K$ below the initial preform temperature. It is seen that the temperature variation in region 1 increases slightly in the beginning and then increases rapidly till η reaches η_f, and continues increasing in region 2 till it becomes zero at a value of $\eta > \eta_f$. By comparing the results to [42], it seems that the convection term strongly affect the temperature variation, as it causes some heat flux at the interface.

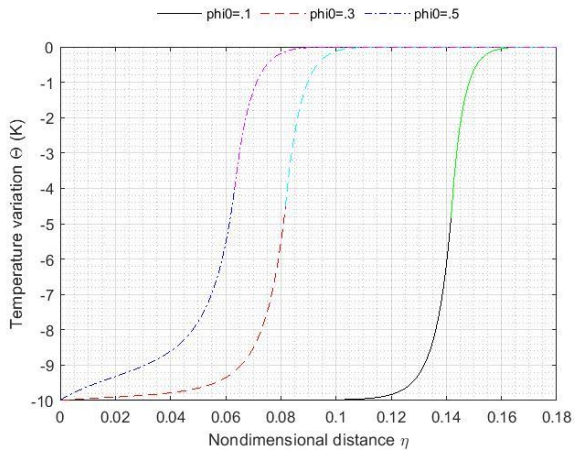

Figure 28 Temperature variation along the infiltration direction

Figure 29 shows the normalized pore fluid pressure $\tilde{p} = p/p_0$ along the infiltration direction. Under an applied pressure of $p_0 = 10\,MPa$, all parameters and the non-dimensional infiltration distance are the same as those in Figure 28. The normalized pore pressure almost

decreases linearly along the infiltration direction and it reaches zero at the infiltration front, where the fluid stops moving. By comparing to [42], it looks that the convection does not affect pressure distribution.

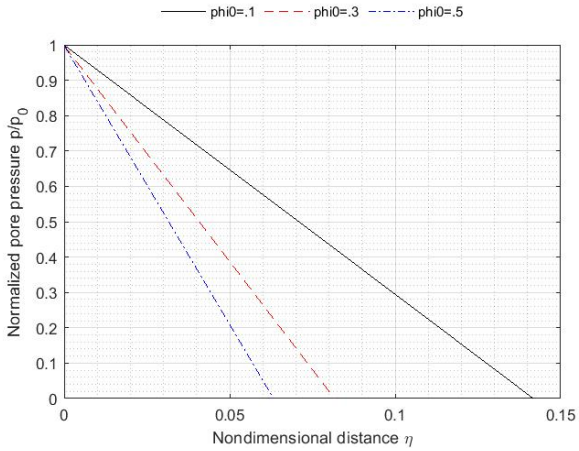

Figure 29 Normalized pore pressure along the infiltration direction

Figure 30 shows the normalized fluid content variation $\zeta/(p_0/K)$ along the infiltration direction under an applied pressure of $p_0 = 10\ MPa$. All parameters and the non-dimensional infiltration distance are the same as those in Figure 28. The fluid content variation is positive and maximum, at the inlet, and it decreases along the infiltration direction. It may reach zero and go below zero as shown in the figure for $\phi_0 = 0.1$ and $\phi_0 = 0.3$, or it may stay positive along the infiltration direction as shown for $\phi_0 = 0.5$. By looking at equation (115), the fluid content variation has a negative constant term, $-\frac{\alpha}{3K}\frac{1+\upsilon}{1-\upsilon}p_0$, which is the same for all values of ϕ_0, a positive term, $\frac{\tilde{S}}{K}p$, which has the same value at the inlet and vanishes at the interface for all values of ϕ_0, and a positive term, $-\omega\alpha_2\theta_1$, which increases with the increase in porosity, and it is the reason of the difference in the behavior of the fluid content variation. The fluid content variation

is completely different than when we ignore the convection term [42], and it seems because the fluid content variation is explicitly function of the temperature variation, equation (115).

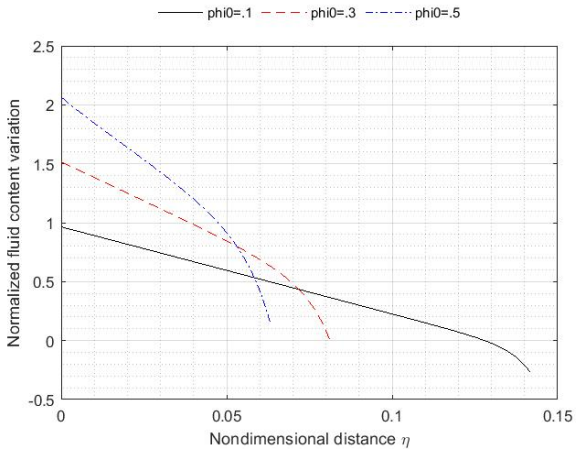

Figure 30 Normalized fluid content variation along the infiltration direction

5 CONCLUSION

This thesis presents self-similar analytical solutions for one-dimensional, linear and radial, isothermal, non-Newtonian fluid flows in a porous solid with two types of boundary conditions; a specified applied pressure and a specified inlet fluid flux factor. It also presents a self-similar numerical solution of one-dimensional, linear, non-isothermal, Newtonian fluid flow in a porous solid with specified applied pressure and temperature boundary conditions considering convection heat transfer. The self-similar solutions are valid for infiltration of a long porous solid by the fluids.

The main conclusions for the isothermal infiltration of porous solid by a non-Newtonian fluid, which can be withdrawn from the results of this thesis, are as follows:

1. The infiltration front is a function of time according to $t^{\frac{n}{n+1}}$, where n is the flow behavior index.
2. The infiltration front advances faster in the linear infiltration than in the radial infiltration.
3. Increasing the flow behavior index *n* for the non-Newtonian fluid increases the non-dimensional infiltration front, while decreasing the solid porosity increases the dimensional and non-dimensional infiltration front.
4. Regarding the pore pressure distribution, the results show that it is almost linear in the linear infiltration, while it is non-linear in the radial infiltration and it drops to zero at the infiltration front.

The main conclusions for the non-isothermal infiltration of porous solid by a Newtonian fluid, which can be withdrawn from the results of this thesis, are as follows:

1. For non-isothermal 1D linear flow of a Newtonian fluid, the dimensional infiltration front varies with time according to $t^{\frac{1}{2}}$. The infiltration front increases with a decrease in the porosity of the porous solid. The pore pressure varies almost linearly from the inlet to the

infiltration front, where it reaches zero. While, the temperature variation increases, when the initial temperature variation is negative, along the infiltration direction and reaches zero at a distance farther than the infiltration front, not at the infiltration front.

2. The infiltration front is a function of time according to $t^{\frac{1}{2}}$.
3. The pore pressure is almost linear along the flow direction and reaches zero at the infiltration front.
4. The fluid content variation is a function of the preform porosity in the non-isothermal linear Newtonian infiltration.
5. The temperature variation increases, when the initial temperature variation at the inlet is negative, non-linearly along the infiltration direction and reaches zero at a distance farther than the infiltration front. Most of the heat transfer happens close to the infiltration front.
6. By comparing the results with that without considering convection [42], it appears that the convection does not affect the infiltration front or the pore pressure. However, the convection does affect the temperature variation and the fluid content variation, which is a function of the temperature variation.

6 REFERENCES

[1] C Ikoku and H Ramey, “Transient Flow of Non-Newtonian Power-Law Fluids in Porous Media,” *Soc. Pet. Eng. J.*, vol. 19, no. 3, pp. 164–174, 1979.

[2] Y Wu, K Pruess, and P Witherspoon, “Flow and Displacement of Bingham Non-Newtonian Fluids in Porous Media,” *SPE Reserv. Eng.*, vol. 7, no. 3, pp. 369–376, 1992.

[3] A. M. Alsofi and Martin Blunt, “Streamline-Based Simulation of Non-Newtonian Polymer Flooding,” *SPE J.*, vol. 15, no. 4, pp. 895–905, 2010.

[4] M Endo Kokubun, F Radu, E Keilegavlen, K Kumar, and K Spildo, “Transport of Polymer Particles in Oil–Water Flow in Porous Media: Enhancing Oil Recovery,” *Transp. Porous Media*, vol. 126, no. 2, pp. 501–519, 2018.

[5] A Mortensen, V Michaud, and M Flemings, “Pressure-infiltration processing of reinforced aluminum,” *JOM*, vol. 45, no. 1, pp. 36–43, 1993.

[6] Y.-S. WU, K. PRUESS, and P. A. WITHERSPOON, “Displacement of a Newtonian Fluid by a Non-Newtonian Fluid in a Porous Medium,” *Transp. Porous Media*, vol. 6, no. 2, 1991.

[7] Karen S. Pedersen and Hans P. Ronningsen, “Effect of Precipitated Wax on Viscosity-A Model for Predicting Non-Newtonian Viscosity of Crude Oils,” *Energy & Fuels*, vol. 14, no. 1, pp. 43–51, 2000.

[8] G. I. Barenblatt, V. M. Entov, and V. M. Ryzhik, *Theory of fluid flows through natural rocks*. Dordrecht: Kluwer, 1990.

[9] X Dong, H Liu, Q Wang, Z Pang, and C Wang, “Non-Newtonian flow characterization of heavy crude oil in porous media,” *J. Pet. Explor. Prod. Technol.*, vol. 3, no. 1, pp. 43–53, 2012.

[10] W Kozicki, A Rao, and C Tiu, “Filtration of polymer solutions,” *Chem. Eng. Sci.*, vol. 27, no. 3, pp. 615–626, 1972.

[11] A. Uscilowska, “Non-Newtonian fluid flow in a porous medium,” *J. Mech. Mater. Struct.*, vol. 3, no. 6, 2008.

[12] T. Sochi, “Flow of Non-Newtonian Fluids in Porous Media,” *Wiley Online Libr.*, vol. 48, no. 23, pp. 2437–2467, 2010, doi: 10.1002/polb.22144.

[13] V. Di and F. Valentina, “Generalized Solution for 1-D Non-Newtonian Flow in a Porous Domain due to an Instantaneous Mass Injection,” *Transp. Porous Media*, vol. 93, no. 1, pp. 63–77, 2012, doi: 10.1007/s11242-012-9944-9.

[14] G. Lewis, “Viscoelastic properties of injectable bone cements for orthopaedic applications: State-of-the-art review,” *J. Biomed. Mater. Res. Part B Appl. Biomater.*, vol. 98B, no. 1, pp. 171–191, 2011.

[15] H Park, M Hawley, and R Blanks, “The flow of non-Newtonian solutions through packed beds,” *Polym. Eng. Sci.*, vol. 15, no. 11, pp. 761–773, 1975.

[16] R. P. Chhabra, J. Comiti, and I. Machac, “Flow of non-Newtonian fluids in fixed and fluidised beds,” *Chem. Eng. Sci.*, vol. 56, no. 1, pp. 1–27, 2001.

[17] J Wannasin and M Flemings, “Fabrication of metal matrix composites by a high-pressure centrifugal infiltration process,” *J. Mater. Process. Technol.*, vol. 169, no. 2, pp. 143–149, 2005.

[18] S. G Fishman and A. K. Dhingra, *Cast reinforced metal composites*. ASM International, 1988.

[19] J. Warren H. Hunt, “Aluminum Metal Matrix Composites Today,” *Mater. Sci. Forum*, vol. 331–337, pp. 71–84, 2000.

[20] V. Michaud and A. Mortensen, “Infiltration processing of fibre reinforced composites: governing phenomena,” *Compos. Part A Appl. Sci. Manuf.*, vol. 32, no. 8, pp. 981–996, 2001.

[21] D. Kopeliovich, *Advances in Ceramic Matrix Composites*. 2014.

[22] T. Ouahbi, A. Saouab, P. Ouagne, S. Chatel, and J. Bre, “Modelling of hydro-mechanical coupling in infusion processes,” vol. 38, pp. 1646–1654, 2007, doi: 10.1016/j.compositesa.2007.03.002.

[23] A Coldea, M Swain, and N Thiel, “Mechanical properties of polymer-infiltrated-ceramic-network materials,” *Dent. Mater.*, vol. 29, no. 4, pp. 419–426, 2013.

[24] H. Pascal, “Rheological behaviour effect of non-newtonian fluids on steady and unsteady flow through a porous medium,” *Int. J. Numer. Anal. Methods Geomech.*, vol. 7, no. 3, pp. 289–303, 1983, doi: 10.1002/nag.1610070303.

[25] H. Pascal, “Rheological effects of non-Newtonian behavior of displacing fluids on stability of a moving interface in radial oil displacement mechanism in porous media,” *Int. J. Eng. Sci.*, vol. 24, no. 9, pp. 1465–1476, 1986.

[26] H. Pascal, “Stability of non-newtonian fluid interfaces in a porous medium and its applications in an oil displacement mechanism,” *J. Colloid Interface Sci.*, vol. 123, no. 1, pp. 14–23, 1988, doi: 10.1016/0021-9797(88)90216-0.

[27] H. Pascal, “Some Self-Similar Flows of Non-Newtonian Fluids through a Porous Medium,” *Stud. Appl. Math.*, vol. 82, no. 1, pp. 1–12, 1990, doi: 10.1002/sapm19908211.

[28] H. Pascal, “Dynamics of moving interface in porous media for power law fluids with yield stress,” *Int. J. Eng. Sci.*, vol. 22, no. 5, pp. 577–590, 1984.

[29] H. Pascal, “On non-linear effects in unsteady flows of non-newtonian fluids through fractured porous media,” *Int. J. Non. Linear. Mech.*, vol. 26, no. 5, pp. 487–499, 1991.

[30] H. Pascal and F. Pascal, “Flow of non-newtonian fluid through porous media,” *Int. J. Eng. Sci.*, vol. 23, no. 5, pp. 571–585, 1985.

[31] S.E. Buckley and M.C. Leverett, “Mechanism of Fluid Displacement in Sands,” *Trans. AIME*, vol. 146, no. 1, pp. 107–116, 1942.

[32] H. J. Welge, “A Simplified Method for Computing Oil Recovery by Gas or Water Drive,” *J. Pet. Technol.*, vol. 4, no. 04, pp. 91–98, 1952.

[33] Zhongxiang Chen and Ciqun Liu, “Self-similar solutions for displacement of non-Newtonian fluids through porous media,” *Transp. Porous Media*, vol. 6, no. 1, pp. 13–33, 1991.

[34] V Di Federico, M Pinelli, and R Ugarelli, “Estimates of effective permeability for non-Newtonian fluid flow in randomly heterogeneous porous media,” *Stoch. Environ. Res. Risk Assess.*, vol. 24, no. 7, pp. 1067–1076, 2010.

[35] R.H. Christopher and S. Middleman, “Power-Law Flow through a Packed Tube,” *Ind. Eng. Chem. Fundam.*, vol. 4, no. 4, pp. 422–426, 1965.

[36] W. KOZICKI, C. J. Hsu, and C. TIU, “Non-Newtonian flow through packed beds and porous media,” *Chem. Eng. Sci.*, vol. 22, no. 4, pp. 487–502, 1967.

[37] J.R.A. Pearson and P.M.J. Tardy, “Models for flow of non-Newtonian and complex fluids through porous media,” *J. Nonnewton. Fluid Mech.*, vol. 102, no. 2, pp. 447–473, 2002.

[38] V. Ciriello and V. Di Federico, “Analysis of a benchmark solution for non-Newtonian radial displacement in porous media,” *Int. J. Non. Linear. Mech.*, vol. 52, pp. 46–57, 2013, doi: 10.1016/j.ijnonlinmec.2013.01.011.

[39] E. Lacoste, O. Mantaux, and M. Danis, “Numerical simulation of metal matrix composites and polymer matrix composites processing by infiltration : a review,” *Compos. Part A Appl. Sci. Manuf.*, vol. 33, no. 12, pp. 1605–1614, 2002.

[40] C Jung, J Jang, and K Han, “Numerical Simulation of Infiltration and Solidification Processes for Squeeze Cast Al Composites with Parametric Study,” *Metall. Mater. Trans. A*, vol. 39, no. 11, pp. 2736–2748, 2008.

[41] H. Prielipp *et al.*, “Strength and fracture toughness of aluminum / alumina composites with interpenetrating networks,” *Mater. Sci. Eng. A*, vol. 197, no. 1, pp. 19–30, 1995.

[42] Z. Jin, “A thermo-poroelasticity theory for infiltration processing of interpenetrating phase composites,” *Acta Mech.*, vol. 229, no. 10, pp. 3993–4004, 2018, doi: 10.1007/s00707-018-2202-7.

[43] M. P. Walsh and L. W. Lake, “APPLYING FRACTIONAL FLOW THEORY TO SOLVENT FLOODING AND CHASE FLUIDS,” *J. Pet. Sci. Eng.*, vol. 2, no. 4, pp. 281–303, 1989.

[44] G. A. Pope, “The Application of Fractional Flow Theory to Enhanced Oil Recovery,” *Soc. Pet. Eng. J.*, vol. 20, no. 3, pp. 191–205, 1980.

[45] W. R. Rossen and et al., “Fractional Flow Theory Applicable to Non-Newtonian Behavior in EOR Processes,” *Transp. Porous Media*, vol. 89, no. 2, pp. 213–236, 2011, doi: 10.1007/s11242-011-9765-2.

[46] D. Ambrosi, “Infiltration through Deformable Porous Media,” *ZAMM*, vol. 82, no. 2, pp. 115–124, 2002.

[47] R. Larsson, M. Rouhi, and M. Wysocki, “European Journal of Mechanics A / Solids Free surface fl ow and preform deformation in composites manufacturing based on porous media theory,” *Eur. J. Mech. / A Solids*, vol. 31, no. 1, pp. 1–12, 2012, doi: 10.1016/j.euromechsol.2011.06.015.

[48] P. C. Dawson, “Flow Properties of Molten Polymers,” *Polym. Sci. Technol. Ser.*, pp. 88–95, 1999.

[49] G. M. Swallowe, *Mechanical properties and testing of polymers*. Dordrecht: Kluwer, 2010.

[50] G. H. R. Kefayati, “Simulation of non-Newtonian molten polymer on natural convection in a sinusoidal heated cavity using FDLBM,” *J. Mol. Liq.*, vol. 195, pp. 165–174, 2014, doi: 10.1016/j.molliq.2014.02.031.

[51] E. Detournay and A. H. D. Cheng, “Fundamentals of poroelasticity,” *Compr. rock Eng. Vol. 2*, vol. II, pp. 113–171, 1993, doi: 10.1016/b978-0-08-040615-2.50011-3.

[52] M. Kurashige, “A thermoelastic theory of fluid-filled porous materials,” *Int. J. Solids Struct.*, vol. 25, no. 9, pp. 1039–1052, 1989, doi: 10.1016/0020-7683(89)90020-6.

[53] N. Noda, R. B. Hetnarski, and Y. Tanigawa, *Thermal Stresses*, 2nd edn. New York: Taylor & Francis, 2003.

[54] Z. H. Jin, K. Tohgo, T. Fujii, and Y. Shimamura, “Double edge thermal crack problem for an interpenetrating phase composite: Application of a matricity-based thermal conductivity model,” *Eng. Fract. Mech.*, vol. 177, pp. 167–179, 2017, doi: 10.1016/j.engfracmech.2017.03.034.

[55] Z. Hashin and S. Shtrikman, “A Variational approach to the theory of the effective magnetic permeability of multiphase materials,” *J. Appl. Phys.*, vol. 33, no. 10, pp. 3125–3131, 1962, doi: 10.1063/1.1728579.

[56] [1]V. Michaud, A. Mortensen and J. Sommer, "Infiltration of fibrous preforms by a pure metal: Part V. Influence of preform compressibility", Metallurgical and Materials Transactions A, vol. 30, no. 2, pp. 471-482, 1999. Available: 10.1007/s11661-999-0337-9.

[57] Vlachopoulos, John, and Nickolas Polychronopoulos. “Basic Concepts in Polymer Melt Rheology and Their Importance in Processing.” *Applied Polymer Rheology: Polymeric Fluids with Industrial Applications*, no. January 2012, 2011, pp. 1–27, doi:10.1002/9781118140611.ch1.

7 BIOGRAPHY OF THE AUTHOR

Hamza Azzam was born in San Luis Obispo, California on June 22, 1994. He was raised in Egypt and graduated from Mit-Rahina High School in 2012. He attended Cairo University and graduated in 2017 with a Bachelor's degree in Mechanical Power Engineering. He started the Mechanical Engineering graduate program at the University of Maine in the Fall of 2018. After receiving his Master's degree, he will continue graduate school at the University of Maine to pursue a Ph.D. degree in Mechanical Engineering. Hamza is a candidate for the Master of Science degree in Mechanical Engineering from the University of Maine in December 2020.